Estimating complex site response function to generate virtual seismogram

R. Amiri Fard[1], S. Parolai[1], F. Panzera[2], F. Romanelli[1]

[1] Department of Mathematics, Informatics, and Geosciences, University of Trieste, Trieste, Italy
[2] Department of Biological, Geological and Environmental Sciences, University of Catania, Catania, Italy

An accurate seismic hazard assessment requires reliable estimates of the local site response. However, commonly used empirical methods have significant limitations. For example, the standard spectral ratio (SSR) requires many high-quality earthquake recordings, making it impractical in regions with low to moderate seismic activity. The horizontal-to-vertical spectral ratio (HVSR) method often fails to accurately determine amplification factors. The noise-based SSR technique can be biased by anthropogenic noise sources. Furthermore, these methods all neglect the complex form of the response, as well as the cross-coupling effects among ground motion components.

This study addresses two key questions: (1) Can a broadband complex site response function (CSRF) be reliably estimated using only ambient seismic noise, and (2) can such a CSRF be used to synthesize realistic virtual seismograms for earthquakes arriving from arbitrary azimuths?

This study, present a new methodology that combines the extended hybrid standard spectral ratio and cross-coupling inversion methods. This approach eliminates the need for earthquake recordings and enables retrieval of the complete 3×3 CSRF tensor. Using three stations, a bedrock station, a soil "bridge" station, and a basin target station, the CSRF has been computed. Then, by convolving the computed CSRF with the earthquake recorded at the bedrock station, the virtual seismograms at the target station are generated.

Corresponding author: rouhollah.amirifard@phd.units.it

Locating seismic event using Distributed Acoustic Sensing (DAS) data and DAS channel correlation: a proof of concept

M. Arcangeli[1], N. Piana Agostinetti[1,2], G. Saccorotti[3], G. Festa[4], R. Pegna[3], E. Bozzi[5], C. Strumia[4], F. Scotto di Uccio[4] and G. Selvaggi[2]

[1]Department of Earth and Environmental Sciences, University of Milano-Bicocca, Italy.
[2]Istituto Nazionale di Geofisica e Vulcanologia, Osservatorio Nazionale Terremoti, Rome, Italy.
[3]Istituto Nazionale di Geofisica e Vulcanologia, Sezione di Pisa, Pisa, Italy.
[4]Universita' di Napoli Federico II, Complesso University Monte S. Angelo, Naples, Ital,.
[5]Universita' di Pisa, Dipartimento di Scienze della Terra, Pisa, Italy.

Introduction

Locating seismic events is a routine activity for monitoring both natural and anthropic seismic activity. Distributed Acoustic Sensing (DAS) technology offers a novel category of seismic data that can be used to improve event location both at regional and local scale (Piana Agostinetti et al., 2022; Bozzi et al, 2024). However, being a distributed measurement along a Fiber Optic (FO) cable, DAS data strongly suffers from error correlation among close-by measurement points (so called DAS channels). Not considering such correlation means assuming DAS measurement for each single channel as an independent measurement, which is obviously not correct. A widely used trick in fiber optic seismology is to "downsample" DAS data and, thus, include in monitoring workflow only a limited number of DAS channels. However, such strategy suffers from two main drawbacks: (a) the number of DAS channels to be used is generally user-defined, meaning that different experts could make different choice in "downsampling" the dataset, and (b) downsampling dramatically reduces the potential of DAS data in locating seismic events, which is based on the full recording of the seismic wavefield at unprecedented dense spatial sampling. In this study, we demonstrate that accounting for error correlation in near-by DAS channels robustly improves seismic event locations, enabling the full use of DAS data in seismic monitoring. Being enable to estimate and to include the full error covariance matrix of a DAS dataset, coupled with a Bayesian approach in seismic event location, gives us the possibility of estimating more accurate and more precise location of seismic events, and more realistic uncertainties in event location. The algorithm is presented using real-world cases, where seismic sources are man-made in known locations.

Data and Methods

We made use of the DAS recordings for two different experiments, at INGV Pisa and INGV Grottaminarda, where a FO cable has been trenched at shallow depth. In Pisa, the FO cable was installed in a a small green area close to INGV building, covering a rectangular area of about 20x30 meters. The seismic source was a hammer hit, repeated 3 times in five different locations, both in

the centre and on a side of the small green area (Figure 1).

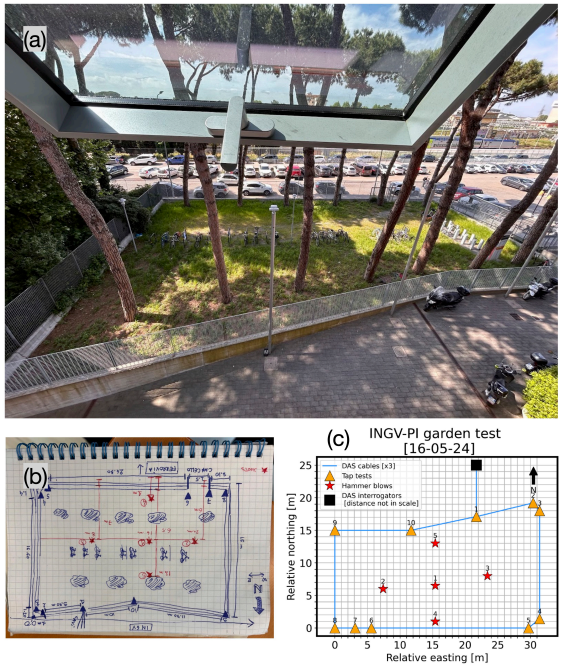

Figure 1: DAS experiment setting in Pisa: (a) green area close to the INGV building where he FO cable was trenched; (b) Sketch of the FO cable geometry from the field notes; and (c) geometry of the FO cable as derived from notes and tap-tests data.

In Grottaminarda, the FO cable was installed outside the INGV building, in a near-by field with a triangular geometry, with sides of length between 50 and 100 meters. The seismic source was a seismic gun, "Energizzatore per seismica Isotta", and 7 shots where operated in different positions relative to the FO cable, both inside and outside of the triangle (Figure 2).

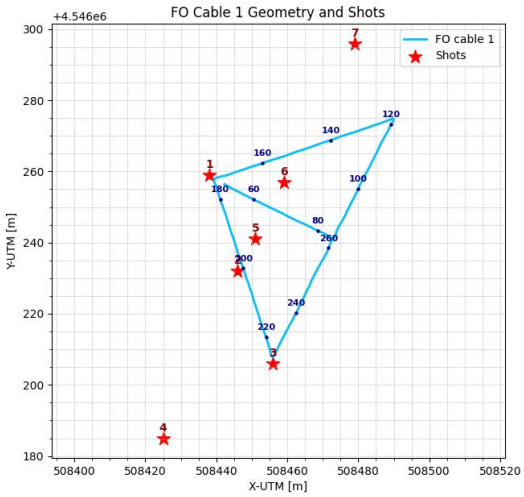

Figure 2: DAS experiment setting in Grottaminarda: geometry of the FO cable as derived from notes and tap-tests data, together with controlled source positions.

As shown in the strain-rate recordings, the full seismic wavefield can be visually inspected in the DAS data, and more seismic phases can be used for locating the event (Figure 3). However, graphical picking tool (e.g. Xdas, Trabattoni, 2024) can introduce correlation in the picking errors, due to the fact that the picking is derived from a continuous line, drawn on the original data.

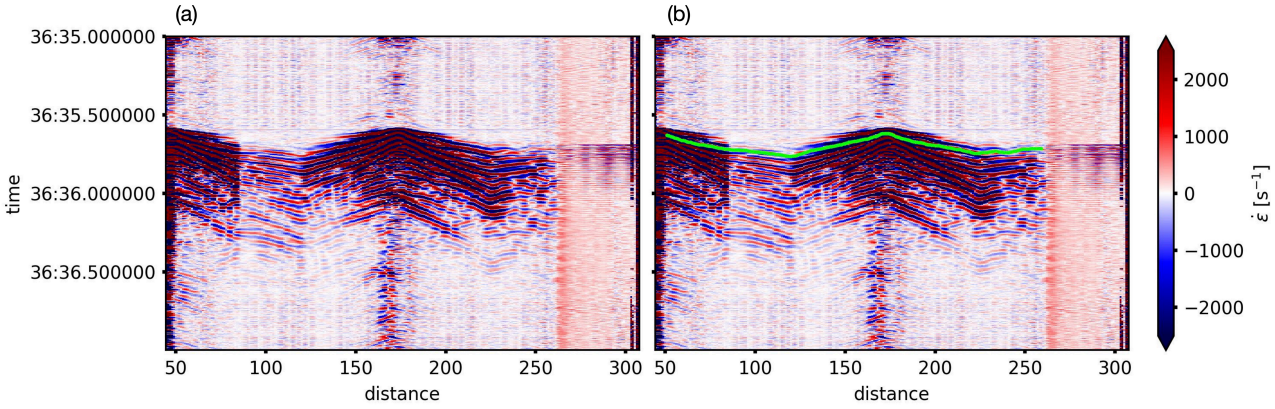

Figure 3: Example of controlled source data recorded in Grottaminarda. (a) the original data; and (b) the graphical picking of a seismic phase that can be seen along the entire cable, used for locating the event.

We perform the location of the controlled-source events using the approach presented in Riva et al. (2021) and modified to account for a full covariance matrix of the errors. Based on a Markov chain Monte Carlo algorithm, such approach is able to extract potential "solutions" (i.e. event

location) from the Posterior Probability Distribution (PPD) of the investigated parameters. Thus, the modification required to the original code was only limited to the computation of the Likelihood of each proposed solution. As a reference, we also perform the location using the original algorithm, where a diagonal covariance matrix of the errors is considered.

Results

Our preliminary results indicate that: (1) errors in DAS data are strongly correlated, as expected, up to a 10-15 channels away in our examples; and (2) the ratio between the estimated uncertainty and the mis-match between true and estimate solutions is generally lower than 2, if error correlation is considered (i.e. it means that location is generally within 2-sigma from the true location), while it is generally larger than 4 when error correlation is not included in the workflow (Figure 4).

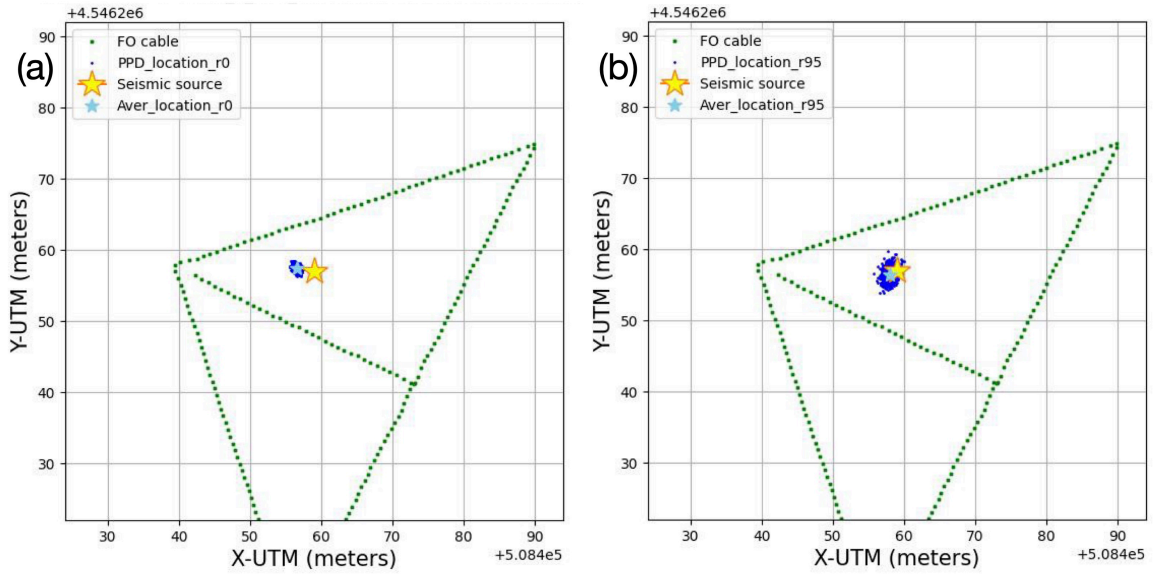

Figure 4: location of a controlled-source event using: (a) diagonal covariance matrix of the error, i.e. considering all DAS measurements as independent; and (b) full covariance matrix of the error, i.e. including correlation in the errors on the P-wave picking for near-by DAS channels. The yellow stars indicate the true position of the source, the blue dots represent potential solutions (i.e. solutions extracted form the PPD), and the green dots show the DAS channel locations.

References

Bozzi E., N Piana Agostinetti, A Fichtner, S Klaasen, A Ugalde, B Biondi, S Yuan, T Dahm, M Isken, P Paitz, F Walter, A F Baird, C Becerril, T Nishimura, J Shen, T Zhu, G Saccorotti (2024) Modelling uncertainty in *P*-wave arrival-times retrieved from DAS data: case-studies from 15 fibre optic cables, *Geophysical Journal International*, 239, 3, 1928–1942, https://doi.org/10.1093/gji/ggae364

Piana Agostinetti, N., A. Villa and G. Saccorotti (2022) Distributed acoustic sensing as a tool for subsurface mapping and seismic event monitoring: a proof-of-concept, *Solid Earth*, 13, 449–468, https://doi.org/10.5194/se-13-449-2022

Riva, F., Piana Agostinetti, N., Marzorati, S., and Horan, C. (2023). The micro-seismicity of Co.

Donegal (Ireland): Defining baseline seismicity in a region of slow lithospheric deformation. *Terra Nova*, 00, 1–15. https://doi.org/10.1111/ter.12691

Trabattoni A. (2024) xdas-dev/xpick: 0.1.0b1 (0.1.0b1). Zenodo. https://doi.org/10.5281/zenodo.13627861

Corresponding author: nicola.pianaagostinetti@unimib.it

A Contribution to the Assessment of DAS Performance with Surface Waves: a case-study from Northern Italy

S. Beretta[1], S. Castellaro[1], N. Piana Agostinetti[2], A. Villa[2], L. Suranna[2]

[1] Dipartimento di Fisica e Astronomia "Augusto Righi", Alma Mater Studiorum - Università di Bologna, Bologna, Italy
[2] Dipartimento di Scienze dell'Ambiente e della Terra, Università di Milano-Bicocca, Milano, Italy

Distributed Acoustic Sensing (DAS), a technology that transforms fiber-optic cables into dense seismic arrays, has rapidly become a widely used tool for a broad range of Earth and environmental studies, both onshore and offshore. With the aim of improving our understanding of DAS instrumental response, this research explores the potential of DAS data for near-surface imaging through surface-wave analysis.

We present results from a case study in northern Italy, at the margins of the Northern Apennines, an area of tectonic interest due to the possible surface emergence of a major fault system, the Stradella thrust, located about 50 km south of Milan. This south-dipping structure represents the western segment of the Pede-Apennine Thrust Front, situated in the rear of the Emilia Arc thrust system.

Regional studies carried out for hydrocarbon exploration, based on industrial seismic reflection profiles and deep well logs, provide valuable insights into the crustal structure and its characteristic fold-and-thrust geometry. However, their resolution decreases in the uppermost few hundreds of meters of the crustal succession. This limitation underscores the need for near-surface imaging, which is essential to assessing the possible tectonic deformation affecting the younger Quaternary deposits in the study area.

Thus, two fiber-optic cables with a total sensing length of about 550 m were deployed at the site, and both active and passive DAS data were analyzed to construct a two-dimensional surface-wave velocity model. The results are compared with those obtained from traditional geophone arrays, including horizontally polarized sensors, in order to evaluate the relationship between the axial strain measured by DAS – its intrinsic DAS observable – and the horizontal ground motion in the same direction recorded by geophones.

At the same site, a single-station ambient-noise survey was conducted to produce contour maps of the main seismo-stratigraphic reflectors using an independent method. Complementary electrical resistivity tomography (ERT) data were also collected.

We discuss the comparison between all datasets, highlighting the potential and limitations of DAS for near-surface characterization, as well as possible directions for future developments.

Data and Resources

The DAS data were collected within the PRIN project “NASA4SHA – Fault segmentation and seismotectonics of active thrust systems: the Northern Apennines and Southern Alps as laboratories for new seismic hazard assessments in northern Italy” (University of Milano-Bicocca research unit, coordinated by A. Tibaldi; Principal Investigator R. Caputo, University of Ferrara)."

The other data were collected from the University of Bologna.

References

Tibaldi, A., de Nardis, R., Torrese, P., Bressan, S., Pedicini, M., Talone, D., Bonali, F.L., Corti, N., Russo, E. & Lavecchia, G.; 2023: A multi-scale approach to the recent activity of the Stradella thrust in the seismotectonic context of the Emilia Arc (northwestern Italy). Tectonophysics Vol. 857, n. 229853. 23 pp, https://doi.org/10.1016/j.tecto.2023.229853

Zhan, Z.; 2019: Distributed Acoustic Sensing Turns Fiber-Optic Cables into Sensitive Seismic Antennas. Seismological Research Letters Vol. 91, n. 1, 1–15, https://doi.org/10.1785/0220190112

Corresponding author: silvia.beretta@unibo.it (S. Beretta)

Viscoacoustic Full Waveform Inversion using Implicit Neural Representation

S. Berti[1], M. Aleardi[1], E. Stucchi[1], A. Tognarelli[1], N. Bienati[2], J. Panizzardi[2], A. Mazzotti[1]

[1] *Dipartimento di Scienze della Terra, Università di Pisa, Italia*
[2] *ENI spa, Milano, Italia*

Introduction

Recovering seismic velocity and attenuation in geologically complex environments remains one of the most demanding problems in full waveform inversion (FWI). In viscoacoustic media, strong intrinsic attenuation, amplitude decay, and phase distortions often coexist with strong low-velocity anomalies, generating shadow zones that significantly limit the reliability of classical deterministic inversions.

The Valhall field provides a synthetic example where a shallow gas cloud induces a marked depression in P-wave velocity (Vp) and a strong reduction in the quality factor (Qp). These effects significantly complicate the joint recovery of Vp and Qp, and conventional grid-based FWI often struggles to produce stable and interpretable attenuation models (Yong et al. 2024).

Implicit neural representations have recently gained attention as a viable alternative to traditional grid-based parametrizations for waveform inversion. Instead of discretizing the subsurface on a fixed mesh, INRs use neural networks that map spatial coordinates to physical properties in a continuous domain. Among these approaches, SIREN networks, based on sinusoidal activations, provide excellent expressivity for oscillatory fields and smooth geophysical structures, while producing high-quality gradients for optimization (Sitzmann et al. 2020). Their continuous formulation makes them resolution-independent, inherently multi-scale, and capable of capturing complex spatial patterns using far fewer parameters than finite-difference grids and employing random starting points.

In this work, we apply an implicit viscoacoustic FWI (IFWI) based on SIREN networks to the synthetic Valhall model. The model contains a pronounced shallow gas cloud producing both a strong velocity depression and an associated attenuation anomaly.

The inversion follows a sequential strategy: first, the Vp is estimated while keeping Qp fixed; then the recovered Vp is held constant while Qp is inverted. This approach mitigates the well-known cross-talk between velocity and attenuation and stabilizes the estimation of Qp, which is highly sensitive to inaccuracies in the velocity model.

To further enhance resolution, we complement IFWI with a short deterministic FWI stage applied to the grid-sampled models. This hybrid strategy combines the stability and regularizing behavior of INRs with the fine-scale resolving power of classical deterministic inversions.

To evaluate the performance of the proposed workflow, we also perform a traditional deterministic viscoacoustic FWI starting from smoothed versions of the true models. This baseline represents an

idealized deterministic scenario and therefore provides a strong benchmark for assessing improvements introduced by IFWI.

Method

The subsurface properties are represented through an implicit neural network $f_\theta(\boldsymbol{x})$, where the parameters θ define continuous functions for Vp and Qp at any spatial coordinate $\boldsymbol{x} = (x, z)$. Two separate SIREN networks are employed, one for Vp and one for Qp. Each network consists of two hidden layers with 128 neurons each, using sinusoidal activations modulated by a frequency factor of 10 that enables accurate representation of high-frequency spatial variations. This architecture provides a balance between expressive capacity and computational efficiency, which is essential for large-scale multi-parameter inversion.

Forward modelling is performed with Devito (Louboutin et al. 2019) using a Standard Linear Solid (SLS) viscoacoustic formulation. Gradients for the wave equation are computed through the adjoint-state method built in Devito, while derivatives with respect to the neural network are obtained by automatic differentiation.

The network takes spatial coordinates as inputs and outputs the physical parameter of interest; the inversion therefore modifies only the network weights, while the model is sampled on demand at the grid nodes required by the numerical solver.

The inversion proceeds in two stages. In the first stage, only Vp is updated, starting from a randomly initialized SIREN network, while Qp is kept fixed at a homogeneous value. After convergence (1000 iterations with Adam optimizer, using a 0.001 learning rate), the recovered Vp is fixed and used to generate viscoacoustic simulations in the second stage, which inverts solely for Qp using an independently initialized SIREN. The use of random initialization for both networks demonstrates the ability of IFWI to shape a physically meaningful subsurface model without relying on informative starting points.

After completion of the IFWI stages, the predicted Vp and Qp models are both refined using a short deterministic inversion phase. We perform 10 iterations on the grid-sampled models, exploiting the accurate gradients available on the numerical grid. This stage enhances the resolution of boundaries, sharpens the attenuation anomaly, and adjusts small-scale features that may be difficult for a low-depth SIREN network to represent.

For comparison, a traditional deterministic viscoacoustic FWI is performed separately, initializing both Vp and Qp from smoothed versions of the true models. This provides an optimistic baseline for assessing the improvement introduced by the implicit formulation.

Results

The true Valhall synthetic model used in this study contains a strong low-velocity anomaly associated with the shallow gas cloud, extending laterally across the central region and producing significant amplitude dimming in the seismic data. The corresponding Qp anomaly is also spatially confined to the gas zone, exhibiting a high attenuation zone that dramatically affects wave propagation. The true models used in this study are illustrated in Figure 1 and serve as a benchmark for evaluating the inversion results.

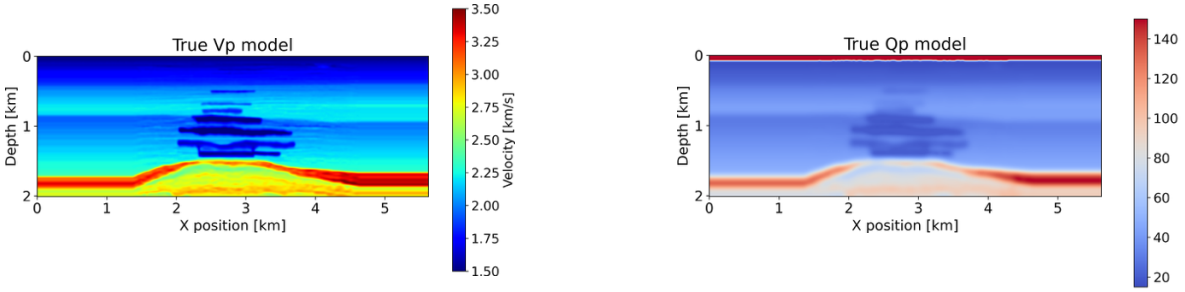

Figure 1 *True Vp and Qp models for the Valhall synthetic gas-cloud case.*

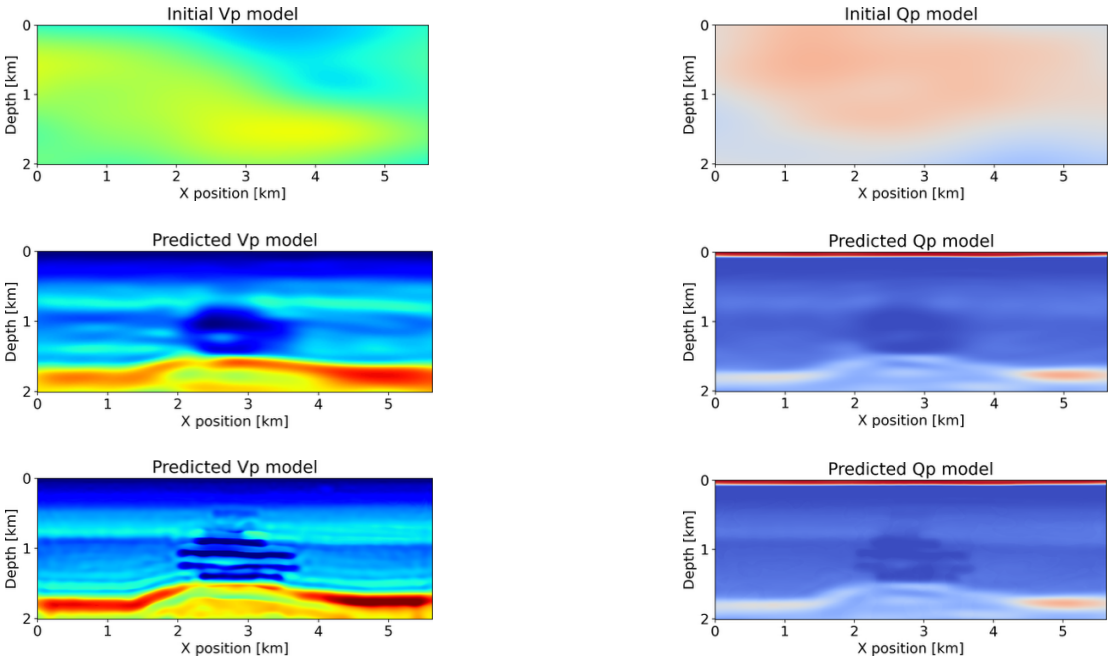

Figure 2 *Initial and predicted Vp and Qp models for the Valhall synthetic experiment using the proposed inversion workflow.*

In the first inversion stage, the IFWI successfully reconstructs the overall geometry of the velocity depression, despite starting from a completely random model. The INR produces a smooth but geologically consistent representation, accurately capturing the lateral position and vertical extent of the gas cloud and showing a good agreement with the true Vp structure (see Figure 2).

The second inversion stage focuses on attenuation, using the predicted velocity as input. The estimated Qp field aligns closely with the true attenuation anomaly (Figure 2). The continuity enforced implicitly by the SIREN network prevents the formation of spurious oscillatory artefacts typically encountered in grid-based multiparameter inversions.

Following the IFWI stages, the 10 iterations of a standard deterministic inversion are used to sharpen the velocity boundaries and to improve the contrast of the attenuation anomaly, adding finer details to the final predictions of both Vp and Qp.

If we compare these results with those obtained through a deterministic baseline inversion that starts from smoothed versions of the true models (Figure 3), we can observe that the predicted Vp model is affected by some artifacts and the low-velocity zone corresponding to the gas cloud is not

perfectly reproduced. For the attenuation, the predicted Qp models is not able to correctly identify the high-attenuation regions, producing diffuse attenuation zones in the central part of the model. Overall, the results obtained with the hybrid approach of IFWI combined with deterministic inversion closely resemble the target fields shown in Figure 1, confirming that the implicit neural approach is capable of capturing both kinematic and amplitude-related information, even when starting from completely random initial models.

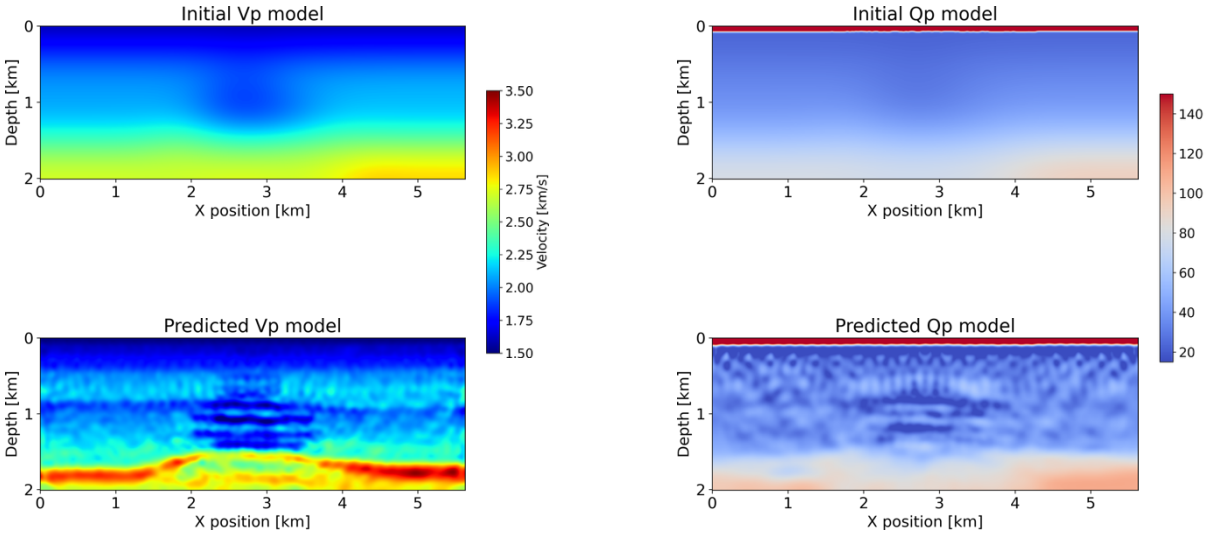

Figure 3 *Initial and predicted Vp and Qp models for the Valhall synthetic experiment using a standard deterministic inversion.*

Conclusions

This study demonstrates that implicit neural representations using SIREN networks provide an effective and robust framework for viscoacoustic FWI in complex geological settings such as the Valhall gas-cloud model. The continuous and resolution-independent representation reduces discretization artefacts, enhances inversion stability and the use of a sequential inversion workflow neglects possible artifacts associated with cross-talk effect between Vp and Qp. Remarkably, even when starting from random initial models, IFWI successfully recovers both the low-velocity zone and the localized high-attenuation anomaly characteristic of the shallow gas cloud. The subsequent deterministic refinement further enhances resolution, compensating for the limited depth of the neural architecture. When compared to a classical deterministic viscoacoustic FWI initialized from smoothed versions of the true models, our proposed approach demonstrates superior reconstruction quality, sharper boundaries and more stable Qp estimation. Thes results highlight the potential of implicit viscoacoustic FWI as a powerful and flexible methodology for multi-parameter imaging in complex, strongly attenuative environments, and provide a promising direction for its application to field-scale datasets.

Possible future developments include exploring deeper SIREN architectures capable of reproducing fine-scale details without the need for a subsequent deterministic refinement step or employing a single joint network to simultaneously invert both Vp and Qp.

Acknowledgements

The results presented in this study were obtained within a research project funded by ENI. We thank ENI for the permission to publish this work. We express our gratitude to Lorenzo Russo and Matteo Caporal from ENI for their valuable assistance and insightful comments.

References

Louboutin, M., Lange, M., Luporini, F., Kukreja, N., Witte, P.A., Herrmann, F.J., Velesko, P. and Gorman, G.J.; 2019: Devito (v3.1.0): an embedded domain specific language for finite differences and geophysical exploration. *Geoscientific Model Development* 12, 1165-1187.

Sitzmann, V., Martel, J.N.P., Bergman, A.W., Lindell, D.B. and Wetzstein G.; 2020: Implicit Neural Representations with Periodic Activation Functions. *Advances in Neural Information Processing Systems*, 33, 7462–7473.

Yong, P., Brossier, R. and Métivier, L.; 2024: Inversion strategies for *Q* estimation in viscoacoustic full-waveform inversion. *Geophysics*, 89(5), R399–R413.

Corresponding author: sean.berti@dst.unipi.it

Crosstalk analysis in Viscoacoustic Full Waveform Inversion

S. Berti[1], M. Aleardi[1], E. Stucchi[1], A. Tognarelli[1], N. Bienati[2], L. Russo[2], J. Panizzardi[2], A. Mazzotti[1]

[1] *Dipartimento di Scienze della Terra, Università di Pisa, Italia*
[2] *ENI spa, Milano, Italia*

Introduction

Understanding how seismic velocity and intrinsic attenuation jointly influence waveforms is fundamental for reliable subsurface imaging, especially in environments affected by strong amplitude distortions and illumination loss. In viscoacoustic full waveform inversion (VFWI), variations in Vp and Qp often generate similar responses in the data, producing strong parameter coupling and significant cross-talk (Yong et al. 2024). In particular, Qp is notoriously difficult to invert because its imprint on seismic data can be partially indistinguishable from that of Vp, leading to parameter leakage, instability, and non-uniqueness.

In order to investigate this behaviour in a controlled environment, we analyse a simple but representative viscoacoustic model and study the mutual influence between Vp and Qp. The background velocity increases linearly with depth and includes a high-velocity anomaly located on the left side of the model, while attenuation is described by a homogeneous background and a localized low-Qp anomaly situated on the right. This spatial separation allows us to observe how the sensitivity of the wavefield responds to each parameter independently, avoiding artificial correlation induced by overlapping anomalies.

To better understand the undelying causes of parameter coupling, we complement the inversion with a controlled sensitivity analysis based on a simplified model parameterization, restricting the problem to only four scalar parameters—the background velocity, the velocity anomaly, the background attenuation and the attenuation anomaly. This enables explicit computation of the Jacobian, Hessian, covariance and correlation matrices.

Results

We consider a simple 2D model where the background Vp increases linearly with depth, and a high-velocity anomaly is embedded in the left portion of the domain. For Qp, the background is homogeneous while a localized attenuation anomaly is placed on the right side of the model. This

configuration ensures that any interaction between the two physical parameters arises exclusively from wavefield physics rather than geometric overlap.

The inversion workflow follows a two-stage process: in the first stage the Vp is updated while Qp is kept fixed at a homogeneous value. Once the recovered velocity stabilizes, it is fixed, and the second stage targets Qp alone. Both stages use the same numerical framework, based on forward and adjoint simulations performed with Devito under a Standard Linear Solid (SLS) attenuation model (Louboutin et al. 2019). This entire two-stage procedure is repeated for three times, allowing a better reconstruction of both the Vp and Qp anomalies.

From the results shown in Figure 1, we can observe how the predicted velocity field accurately reproduces the velocity anomaly in the correct position while the Qp anomaly has no influence in the Vp prediction. For the Qp prediction instead, the inversion is able to accurately reproduce the Qp anomaly, but some artifacts arise in correspondence of the Vp anomaly.

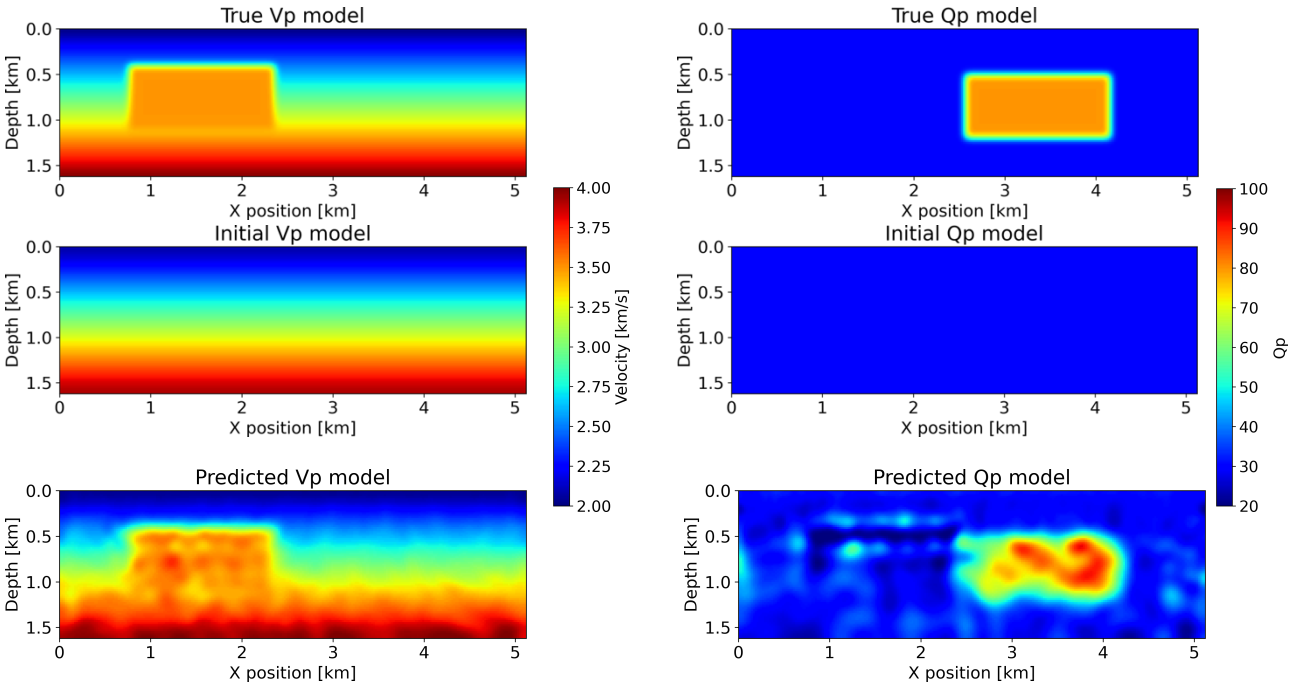

Figure 1. *True, initial and predicted Vp and Qp models.*

If we have a look to the gradient maps related to Vp and Qp (Figure 2), we can observe how the Vp anomaly is visible in the map associated to the Qp at the final iteration of the inversion, confirming the cross-talk between Vp and Qp that affects the FWI predictions.

To better investigate the behavior observed in the sequential FWI, a complementary sensitivity analysis is carried out. The model is parameterized by four different variables: background Vp, Vp anomaly, background Qp and Qp anomaly. This reduced framework makes it possible to interpret the influence of each parameter independently. The Jacobian is then explicitly computed by introducing small perturbations to each parameter and evaluating the corresponding data misfit through viscoacoustic simulations. From the Jacobian, the Hessian, covariance and correlations

matrices are derived, providing a clear interpretation of parameter dependency and uncertainty distribution.

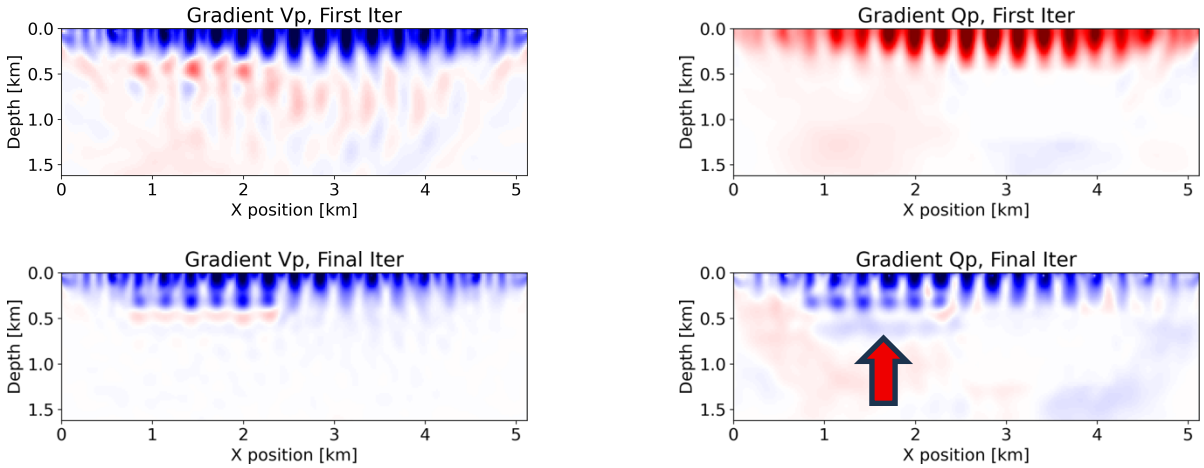

Figure 2. *Gradient maps associated with Vp and Qp, respectively, extracted at the first and last iteration of the FWI workflow. The red arrow highlights the Vp anomaly effect visible in the gradient map associated with the Qp.*

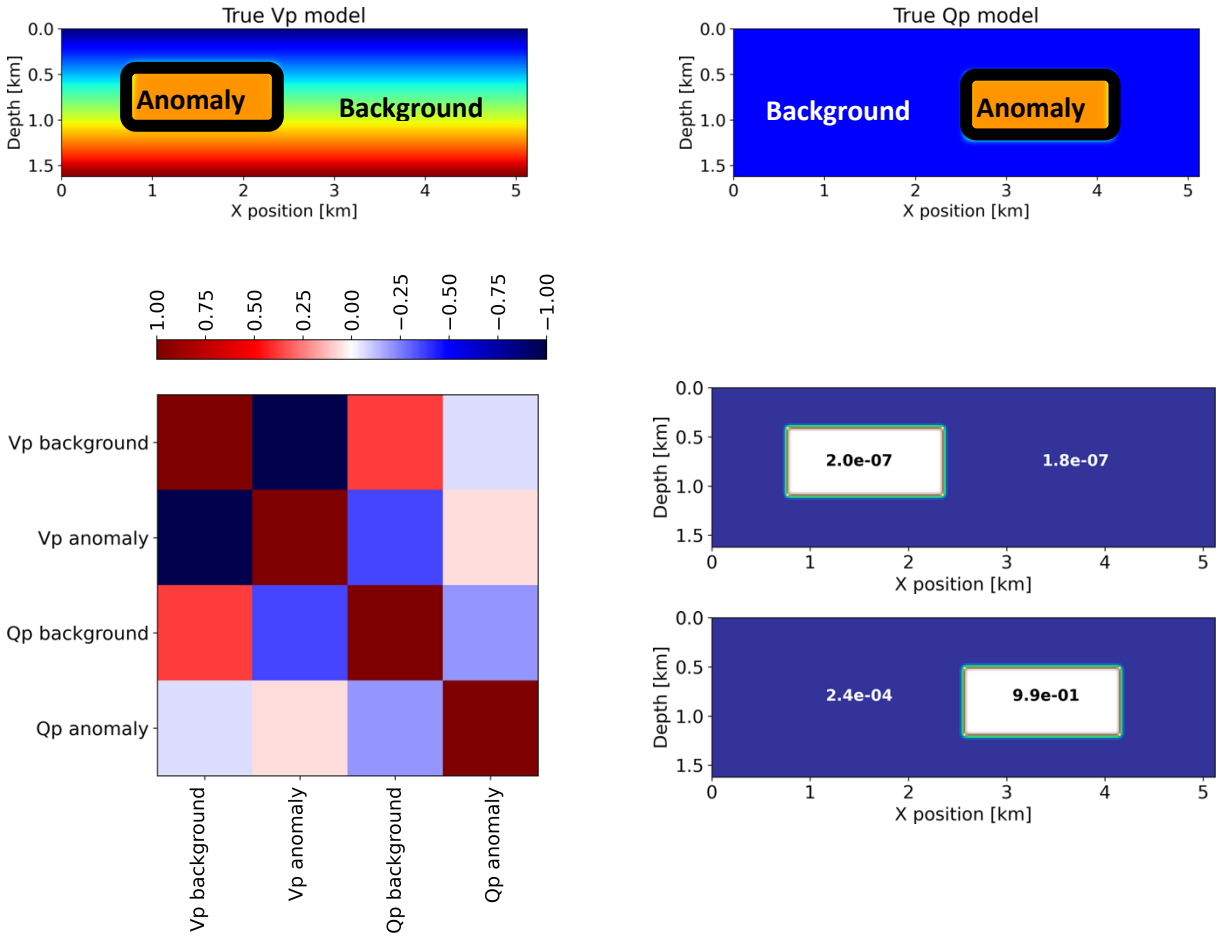

Figure 3. *On top, the simplified four-parameter model used for sensitivity analysis; on the bottom, the correlation matrix and the variance values associated to each parameter.*

This sensitivity analysis reveals strong asymmetry in the way Vp and Qp influence seismic data. The correlation matrix shown in Figure 3 clarifies the coupling between different model parameters. The attenuation anomaly exhibits significant correlations with both velocity components, indicating that attenuation estimates are easily contaminated by velocity mismatches.

The covariance values reveal a striking difference between the resolvability of velocity and attenuation. The variances associated with background velocity and velocity anomaly are relatively small (of the order of 1e-7), confirming that velocity is well constrained by the data. In contrast, the variance associated with the attenuation background reaches approximately 1e-4 and the attenuation anomaly shows a variance close to 1, indicating much higher uncertainty. These values demonstrate that attenuation is fundamentally much more difficult to constrain.

Conclusions

This simplified four-parameter experiment provides a clear and quantitative demonstration of the inherent crosstalk between velocity and attenuation in viscoacoustic FWI. The sensitivity analysis provides an intuitive explanation for this behaviour, showing that velocity is strongly constrained while attenuation is characterized by much larger uncertainty and strong correlation with velocity variations.

The asymmetric coupling revealed by the correlation and covariance analyses shows that attenuation cannot be reliably recovered without strong regularization, low-frequency information or additional prior constraints. These results help explain the instability and noise amplification commonly observed in practical Qp inversions and underline the need for careful parameterization and inversion strategies when simultaneously recovering Vp and Qp in viscoacoustic FWI.

Acknowledgements

The results presented in this study were obtained within a research project funded by ENI. We thank ENI for the permission to publish this work.

References

Louboutin, M., Lange, M., Luporini, F., Kukreja, N., Witte, P.A., Herrmann, F.J., Velesko, P. and Gorman, G.J.; 2019: Devito (v3.1.0): an embedded domain specific language for finite differences and geophysical exploration. *Geoscientific Model Development* 12, 1165-1187.

Yong, P., Brossier, R. and Métivier, L.; 2024: Inversion strategies for *Q* estimation in viscoacoustic full-waveform inversion. *Geophysics*, 89(5), R399–R413.

Corresponding author: sean.berti@dst.unipi.it

The multi-homogeneous theory applied to the imaging of potential fields data

L. Bianco, M. Fedi

Università degli Studi di Napoli "Federico II

The fields generated by ideal sources are homogeneous functions by a constant integer degree, *n*, which is -3, -2, -1 and 0 respectively for spheres, dykes, sills, and contacts.

However, when dealing with geological source distributions and their fields, the homogeneity equation is not satisfied. Instead, they exhibit "multi-homogeneity," it is to say that degree of homogeneity is not fixed but is dependent on the distance from the source. Consequently, *n* often assumes fractional values and varies locally with observation positions.

From this, we integrate multi-homogeneity theory into the Depth from Extreme Points (DEXP) method (Fedi, 2007). This imaging technique was defined for the aforementioned class of 'ideal sources', the proposed integration expands the DEXP application to complex sources, without the need of assuming the ideal sources as representative of the real-world distributions.

The proposed technique is tested on synthetic and real cases. The multi-homogeneous DEXP exhibits a significantly improved recovery of the source geometry, thus allowing also a conversion from DEXP image to physical parameter distribution.

References

Fedi, Maurizio. "DEXP: A fast method to determine the depth and the structural index of potential fields sources." Geophysics 72.1 (2007): I1-I11.

On the Meaning of the Mapping Function Ξ for the Direct MT Data Transform into 1D Resistivity Models

Oscar I. Calderon Hernandez[1], L. Rondoni[2], E.C. Slob[3], L.V. Socco[1,3]

[1] Dipartimento di Ingegneria dell'Ambiente, del Territorio e delle Infrastrutture, Politecnico di Torino, Torino, Italy.

[2] Dipartimento di Scienze Matematiche "G. L. Lagrange", Politecnico di Torino, Torino, Italy.

[3] Faculty of Civil Engineering and Geosciences, Delft University of Technology, Delft, Netherlands.

Introduction

The magnetotelluric (MT) method is a passive geophysical prospecting technique that measures the Earth's response to the diffusion of natural occurring electromagnetic (EM) fields. To derive the subsurface resistivity data inversion techniques are commonly used, however these approaches are ill-posed problems as different resistivity distributions can generate equivalent surface responses.

Previous works have proposed different approaches to tackle the non-linearity of the inverse problem for MT data. In particular, Calderon Hernandez et al. (2026) developed a method in which by defining a 1D cumulative resistance model of the subsurface a mapping function Ξ can be established between the 1D resistivity model and its corresponding MT data. This mapping relationship was used to train a neural network $\hat{\Xi}$ that directly transforms MT data into a 1D resistivity model of the subsurface without requiring a-priori information nor iterative processes.

In this work we explore the physical meaning of the mapping function Ξ, by analyzing its relationship with the attenuation of the electromagnetic field in a layered medium and by comparing it with the conventional skin-depth δ. Furthermore, to evaluate the quality of the solutions provided by the mapping network $\hat{\Xi}$, we explore the solution space associated with the inversion of 1D synthetic MT data. This analysis allows us to determine the position of the network's prediction within the inversion manifold, highlighting the mapping network $\hat{\Xi}$ robustness in addressing the non-uniqueness of the 1D inversion for MT data.

Method

W simulated MT data, to be referred as "measured data", from a 1D resistivity model, to be referred as "true model" (Figure 1a), using the python routine *empymod* provided by Werthmüller (2017). We then computed a resistance model of the subsurface following the approach depicted by Calderon Hernandez et al. (2026) defining the resistance model $R(z)$ as

$$R(z) = \frac{1}{S(z)} \tag{1}$$

where $S(z)$ is the longitudinal conductance.

Using the real component of the wave impedance $\Re\left(Z_{xy}(f)\right)$ from the data, and the resistance model, we searched for all the (z, f) pairs for which $\Re\left(Z_{xy}(f)\right) = R(z)$ (Figure 1b), retrieving the mapping function Ξ (Figure 1c).

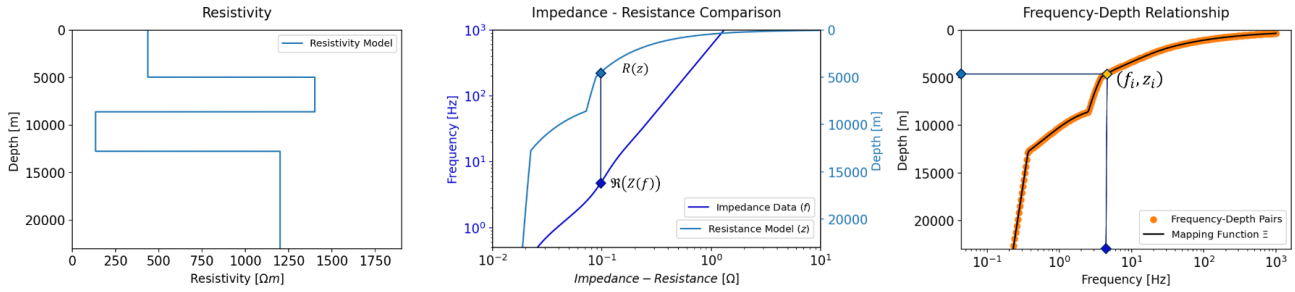

(a) (b) (c)

Figure 1: Proposed layered resistivity model (a). Data and model matching for a given data point (b). Frequency-depth pairs for all data points and the mapping function Ξ between data and model (c).

We then computed the attenuation of the electromagnetic field (Figure 2) for the model in Figure 1a following the approach proposed by Jones (2006) in which the amplitude of the electromagnetic field at each depth is defined as

$$A_{xy}(z) = \sqrt{\frac{|E_x(z)||H_y(z)|}{|E_x(0)||H_y(0)|}} \tag{2}$$

where $|E_x(z)| = \sqrt{E_x E_x^*}$.

Furthermore, to evaluate quality of the 1D resistivity models predicted by the mapping network $\hat{\Xi}$ within the non-unique MT inverse problem solution space, we conducted a global exploration of the solution space using a random search approach. An ensemble of 1D resistivity models and their corresponding MT data were simulated. For each simulated MT data in the ensemble, we computed the data misfit between the simulated and measured data and compared this distribution with the misfit obtained from the mapping network $\hat{\Xi}$.

Results

Physical Meaning of the Mapping Function Ξ

To show the physical meaning of the mapping function Ξ we plotted it on the electromagnetic attenuation field shown in Figure 2 (white) and compared it with the conventional skin depth for MT data (red), defined as

$$\delta = \sqrt{\frac{2\,\rho_{App}}{\mu_0\,\omega}}. \tag{3}$$

Where ρ_{App} denotes the apparent resistivity. In addition, we compared the mapping function Ξ with the true skin depth (blue), defined as the point in which $A_{xy}(f) = 1/e$ for each point in depth.

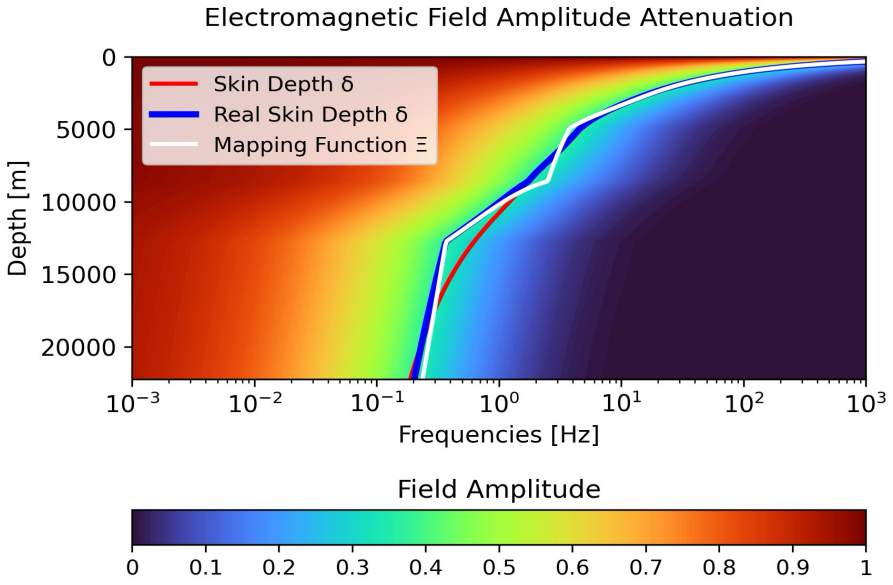

Figure 2: Attenuation field for the layered resistivity model depicted in Figure 1a. Theoretical skin depth computed by using eq. (3) in red. Real skin depth in blue. Mapping function Ξ in white.

The results demonstrate that the mapping function Ξ follows closely the real skin depth, and that its behavior can be directly associated to the resistivity properties of the model in Figure 1a. In particular, the mapping function Ξ captures a dynamic sensitivity of MT data that depends on the resistivity structure of the subsurface, this can be attributed to the fact that Ξ represents a resistivity-dependent, dynamic investigation depth which cannot be depicted by the conventional skin-depth.

Validity of the Mapping Network $\hat{\Xi}$ Results in the Solution Space

To assess quality of the results from the mapping network $\hat{\Xi}$ within the global solution space, we randomly generated 5000 different 1D resistivity models. And for each model, we simulated its corresponding MT data using the forward model *empymod* and we evaluated the data fitting using the normalized root-mean Square (nRMS) error of the complex impedance Z, defined as

$$nRMS = \sqrt{\frac{1}{m}\sum_{i=1}^{m}\frac{|Z_{meas}(f_i) - Z_{sim}(f_i)|^2}{|Z_{meas}(f_i)|^2}}. \quad (4)$$

where m is the number of data points, and Z_{meas} and Z_{sim} denote the measured and simulated complex impedances, respectively. The distribution of misfits obtained from the ensemble of simulated models was then compared with the misfit associated to the resistivity model predicted by the mapping network $\hat{\Xi}$ (red cross) in Figure 3. All compared relative to the misfit of the true resistivity model (blue diamond).

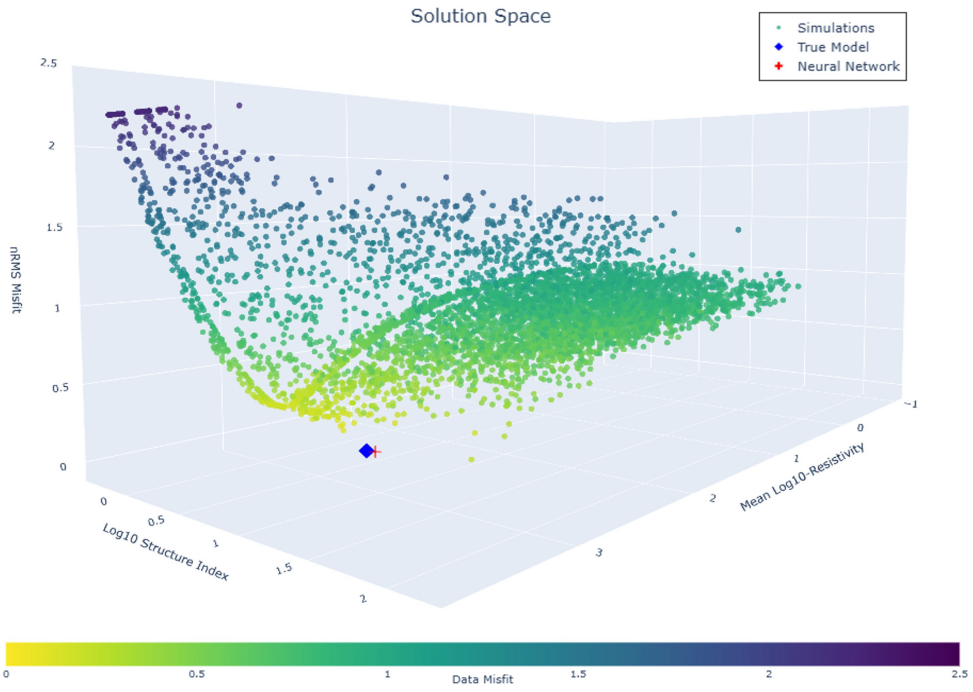

Figure 3: Misfit associated to the solution space for 5000 1D resistivity models. The x-asis represent mean log10-resistivity of all the layers within one model, the y-axis the log10-structure index (total arc length of the resistivity profile), and the z-axis the nRMSE between simulated and measured data (eq. 4). The red cross depicts the results of the mapping network $\hat{\Xi}$ and the blue diamond depicts the true resistivity model.

The validity of the prediction from the mapping network $\hat{\Xi}$, is confirmed by its projection into the solution space. This result has the lowest misfit between simulated and measured data, and the properties of the predicted resistivity model are in agreement with those of the true resistivity model showing the robustness of the mapping network $\hat{\Xi}$.

Conclusions

We investigated the physical meaning of the mapping function Ξ by analyzing its relationship with electromagnetic field attenuation in a 1D layered Earth. By comparing the mapping function Ξ with both the conventional skin depth and the true skin depth for MT data we demonstrated that the mapping function Ξ closely follows the real skin depth and offers a sound data-driven representation of the real depth of investigation of 1D MT measurements.

Furthermore, the robustness of the mapping network $\hat{\Xi}$, was validated through a global solution space analysis based on a random ensemble of 1D resistivity models. The resistivity model predicted by $\hat{\Xi}$, is projected into the region of lowest misfit within the solution space, and its properties are in agreement with the true resistivity model. This result demonstrates that the proposed mapping network $\hat{\Xi}$, not only mitigates the non-uniqueness inherent to 1D MT inversion but also reliably retrieves physically meaningful models, confirming the effectiveness of the approach developed by Calderon Hernandez et al. (2026).

References

Calderon Hernandez, O.I., Rondoni, L., Slob, E. and Socco, L. [2026] Direct MT data transform into 1-D resistivity models: a new approach based on cumulative resistance models. *Geophysical Journal International*, 244(1), ggaf425.

Jones, A.G. [2006] Electromagnetic interrogation of the anisotropic Earth: Looking into the Earth with polarized spectacles. *Physics of the Earth and Planetary Interiors*, 158(2-4), 281–291.

Werthmüller, D. [2017] An open-source full 3D electromagnetic modeler for 1D VTI media in Python: empymod. *Geophysics*, 82(6), WB9–WB19.

Corresponding author: oscar.calderon@polito.it

Joint inversion of inductive and galvanic data: significant resolution improvement honouring both data types – 3D EM and 2D DCIP

J. Chen[1], Francesco Dauti[1], G. Fiandaca[1]

[1]The EEM Team for Hydro & eXploration, Department of Earth Sciences "Ardito Desio", University of Milano, Milano (Italy).

Abstract

In Signora et al. (2025), we demonstrated that the joint 1D electromagnetic (EM) and 2D DCIP (Direct Current resistivity and Induced Polarization) inversion achieves a significant improvement in resolution, as validated by logging data, still honouring both datasets. However, the joint inversion presents much more structure than the independent inversion. Are we certain that this structure is fully compatible with 3D modeling? Would it be possible to carry out a joint inversion of EM and DCIP data also in the presence of strong polarization effects? To answer these challenges, we developed a 3D-EM and 2D DCIP joint inversion scheme capable of modeling IP in both EM and DCIP data with the same polarization model, i.e. the maximum phase angle (MPA) reparameterization of the Cole-Cole model. The key feature of this joint 3D EM/2D DCIP inversion scheme is the decoupling of inversion and forward meshes, together with the possibility to tailor the 3D EM forward meshes to the modelled EM systems, with mesh refinements dependent on the size of the EM system footprint and penetration depth and modelling to the Tx shape. We implemented this new development on two distinct datasets: one for hydrogeological characterization and the other for mineral exploration.

I Introduction

Geophysical electromagnetic (EM) and electrical methods play significant roles in hydrogeological exploration and mineral resource investigations. EM methods can efficiently conduct large-scale resistivity surveys, such as airborne electromagnetic (AEM) methods. When considering the induced polarization (IP) effect, the EM methods can also delineate the distribution of shallow subsurface chargeable anomalies. Electrical methods, such as direct current (DC) resistivity and time domain induced polarization (TDIP) techniques, employ surface electrode arrays to obtain subsurface resistivity and polarization information. Although electrical methods exhibit lower survey efficiency compared to EM techniques, they offer good exploration resolution, making them well-suited for localized geological investigations. However, both electrical and EM methods suffer from non-uniqueness in data inversion, meaning multiple distinct subsurface models can fit the measured data. To mitigate the non-uniqueness issue in inversion, researchers began exploring the use of data

collected from multiple geophysical methods to derive a robust model capable of simultaneously fitting diverse datasets. This approach is known as joint inversion.

Joint inversion fundamentally differs from traditional integrated interpretation. Integrated interpretation merely combines the inversion results of independent methods without leveraging the synergistic potential of cross-method observational data, leaving its quality dependent on the interpreter's expertise. In contrast, joint inversion capitalizes on shared physical parameters (e.g., resistivity) across different geophysical methods to simultaneously process diverse datasets, thereby achieving superior inversion resolution compared to individual methods. For electrical and EM methods, EM techniques generate currents through induction, primarily sensing horizontal resistivity variation characteristics, while the electrical method measures the vertical-horizontal geometric mean resistivity by injecting currents directly into the ground. Their complementary sensitivities to conductors (EM) and resistances (DC), combined with shared resistivity parameters (both can be extended to model IP effects), make joint inversion particularly valuable.

Most of the existing studies on joint inversion of electrical and EM methods focus on resistivity parameters, and the modeling physical kernel is mostly based on a 1D layered earth approximation. In Signora et al. (2025), we show that joint 1D EM and 2D DCIP achieves a significant increase in resolution, still honouring both datasets. Since the research cases demonstrated by Signora et al. (2025) involve a weak-to-mild polarization for hydrogeological purposes, it is essential to explore whether the joint inversion remains applicable under conditions of strong polarization in geological settings. For these reasons, in this study we present a 2D joint inversion framework combining three-dimensional (3D) EM and 2D DCIP forward physical kernel to simultaneously recover resistivity and IP parameters based on the EEMverter platform (Fiandaca et al., 2024).

II Method and Theory

In our 3D EM numerical simulation approach, we have adopted a primary-secondary field separation technique. Unlike the traditional total field computation strategy, this method does not require dense meshing near the source and has a smaller footprint area, conducive to the substantial conservation of computational resources. Applying Dirichlet boundary conditions, the frequency domain electromagnetic curl-curl equation is (Chen et al., 2025):

$$\int_{\Omega}(\nabla \times \mathbf{N} \cdot \nabla \times \mathbf{E}^{s} - i\omega\mu(\sigma^{s} + \sigma^{p})\mathbf{N} \cdot \mathbf{E}^{s})d\mathrm{V} = \int_{\Omega}(i\omega\mu\sigma^{s}\mathbf{N} \cdot \mathbf{E}^{p})d\mathrm{V}\,, \qquad (1)$$
$$\boldsymbol{E}_{s}|_{\Omega} = 0.$$

The 2D galvanic DC and full-decay IP modelling are also calculated in the frequency domain, neglecting electromagnetic induction. For a point source with (zero-phase) current I, this problem can be defined by Poisson's equation and solved through Fourier transformation in the strike (y) direction:

$$\frac{\partial}{\partial x}\left(\sigma^{*}\frac{\partial \phi^{*}}{\partial x}\right) + \frac{\partial}{\partial z}\left(\sigma^{*}\frac{\partial \phi^{*}}{\partial z}\right) - \lambda^{2}\phi^{*}\sigma^{*} = -I\delta(x)\delta(z) \qquad (2)$$

where ϕ^* and σ^* are the Fourier-transformed complex potential and the complex conductivity respectively, λ is the Fourier transformation variable and δ represents the Dirac delta function. The differential equation is solved by using the finite element method, applying the Neumann- and Dirichlet-type boundary conditions. For further details regarding the 2D DCIP modeling, see Fiandaca et al. (2013). The forward computations for both electrical and EM methods are performed in the frequency domain, and the time domain solution is obtained by a fast Hankel transformation.

III Results

As shown in Figure 1, the study area is in the Ossa-Morena Zone of southern Portugal. The AEM data from this region exhibits sign reversal phenomena caused by strong IP effects (Fig. 1c). On the ground, two follow-up DCIP lines were carried out in the Odivelas area, with the ABEM Terrameter LS 2 system in full-waveform acquisition.

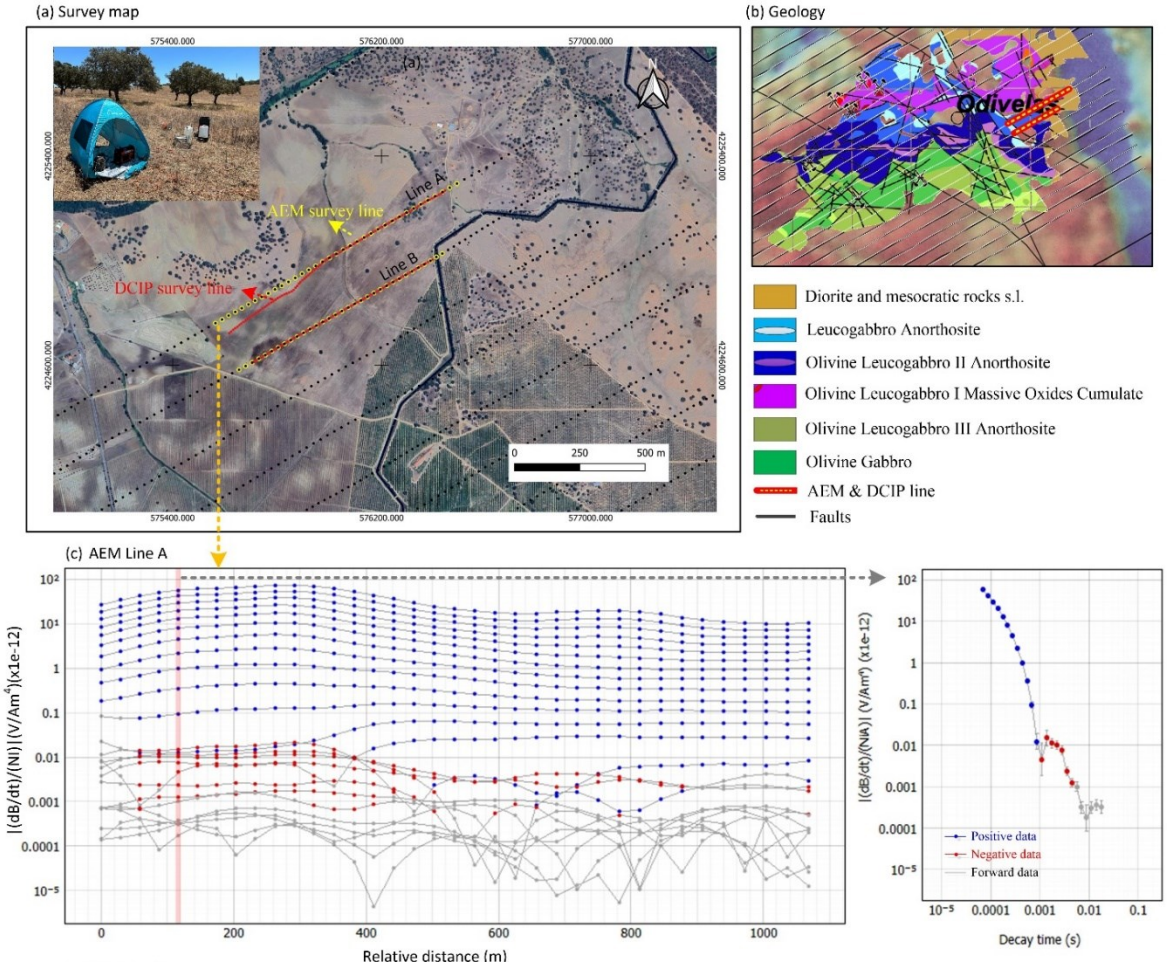

Fig. 1. DCIP and AEM survey line distribution and acquisition data. (a) Map of the Beja survey line; (b) Reference geology; (c) Example of AEM data with IP effects.

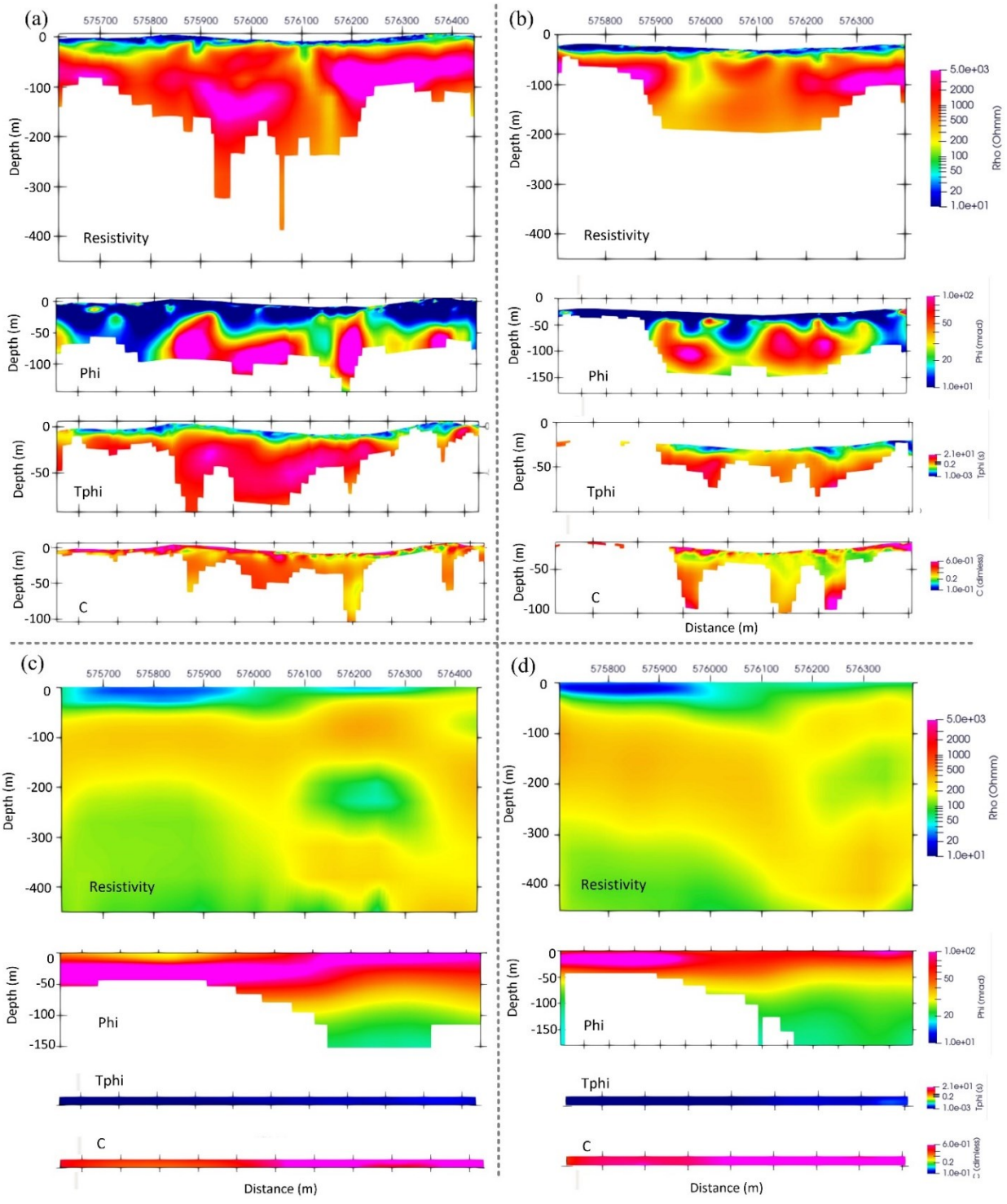

Fig. 2. Comparison of independent inversion results for the Beja survey lines. (a) 2D DCIP independent inversion for Line A; (b) 2D DCIP independent inversion for Line B; (c) AEM independent inversion for Line A (1D EM kernel); (d) AEM independent inversion for Line B (1D EM kernel). From top to bottom: the resistivity, the chargeability phase, the phase relaxation time and the frequency exponent.

Figure 2 presents the results of independent inversion based on the MPA parameterization model. It is evident that both DCIP and AEM exhibit significant correlations in the IP parameters inversion results along two adjacent survey lines. The DCIP resistivity results, with a DOI of approximately 200 meters, reveal a distribution pattern in the shallow subsurface characterized by an initial low-resistivity layer followed by a high-resistivity zone, corresponding to the soil layer and gabbro layer,

respectively. The DCIP chargeability phase indicates a strong polarization anomaly in the region from 50 to 150 meters below the surface, predominantly concentrated on the eastern side of the survey line. The AEM resistivity results (Figs. 2c & 2d), with a higher DOI of about 450 meters, demonstrate that the high-resistivity layer extends both towards the shallow surface and deeper sections on the eastern side of the survey line, forming a low-resistivity zone in the middle, which is hypothesized to be associated with an oxide accumulation layer. The resolution of the AEM chargeability phase is inferior to that of DCIP, only showing a strongly polarized parameter layer in the shallow subsurface, with the thickness and intensity of the polarized layer decreasing from the western to the eastern side.

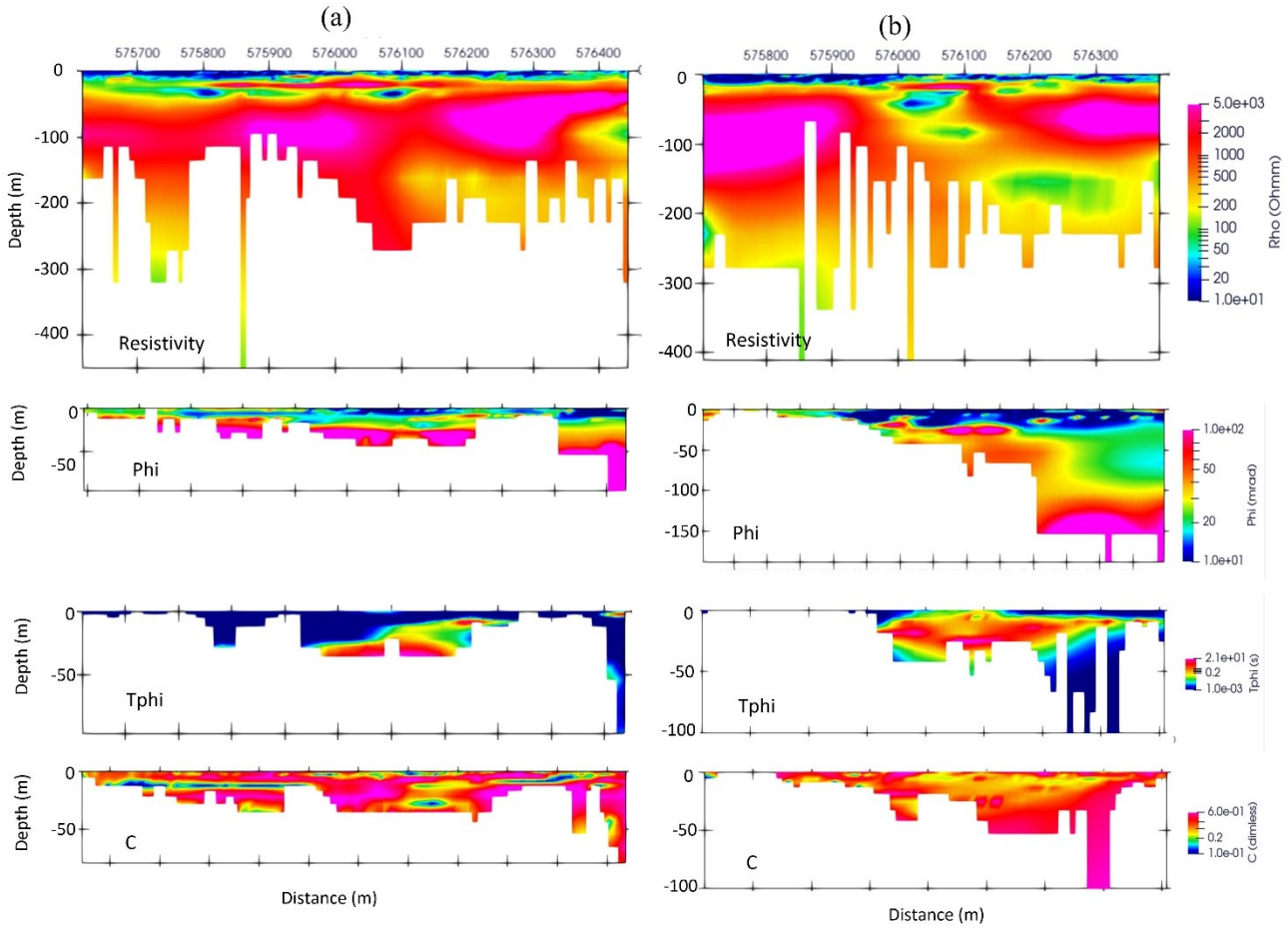

Fig. 3. Comparison of 2D joint E&EM inversion results for the Beja survey lines. (a) Joint inversion results for Line A; (b) Joint inversion results for Line B. From top to bottom: the resistivity, the chargeability phase, the phase relaxation time and the frequency exponent.

Figure 3 shows the 2D joint inversion results of the two survey lines. Within the DOI range, the joint inversion demonstrates superior spatial resolution, with more detailed delineation of resistivity and IP parameters in the shallow subsurface intrusive rock layer. Additionally, the chargeability phase from the joint inversion reveals that the subsurface strongly polarized zone gradually extends deeper from survey Line-A to survey Line-B. In terms of phase relaxation time, the joint inversion reveals that the effective DOI is primarily concentrated from the central to the eastern part of the survey lines. It consistently highlights the characteristic of coarse-grained mineralized zones being semi-enclosed by fine-grained media, which may be related to intrusive rock layers. Regarding the

frequency exponent, Survey Line A exhibits more localized band-like strong variations, suggesting the presence of multiple types of mineralized zones.

IV Conclusions

In this work, we presented a novel inversion scheme for the joint inversion of electrical and electromagnetic (E&EM) datasets with modelling of induced polarization and 3D EM kernel. The results from the mineral exploration case study indicate that the joint inversion of E&EM data is also applicable under geological conditions characterized by strong polarization parameters. More importantly, compared with independent inversion models, the E&EM joint inversion model is not merely a hybrid of individual results but rather a solution that significantly enhances subsurface resolution. This improvement stems from the complementary spatial sensitivities of DCIP and EM methods.

Acknowledgments

This study has been carried out within the Horizon Europe project SEMACRET.

References

Chen, J., Dauti, F., Wertich, V., Viezzoli, A., Zhang, B., & Fiandaca, G., 2025. 3D EM inversion considering induced polarization effect. Geophys. J. Int. https://doi.org/10.1093/gji/ggaf462.

Fiandaca, G., Chen, J., Zhang, B., et al., 2024. Closing the gap between galvanic and inductive induced polarization: EEMverter, a new modelling tool for Electric and Electromagnetic data. GNGTS 2025, 11-14 February 2025, Bologna, Italy.

Fiandaca, G., Ramm, J., Binley, A., Gazoty, A., Christiansen, A.V., Auken, E., 2013. Resolving spectral information from time domain induced polarization data through 2-D inversion. Geophys. J. Int., 192, 631–646. https://doi.org/10.1093/gji/ggs060.

Signora, A., et al. "Joint inversion of Electrical and Electromagnetic data–Part I: unprecedented resolution improvements." *NSG 2025: 31st Meeting of Environmental and Engineering Geophysics*. Vol. 2025. No. 1. European Association of Geoscientists & Engineers, 2025

Corresponding author: Jian.Chen@unimi.it

A synthetic study of the cosmic ray neutron sensing detector response to heterogeneous soils and moisture content distribution

V. Cioffi[1], G. Cassiani[1], L. Peruzzo[1]

[1] *Department of Geosciences, University of Padua, Padua, Italy*

The accurate quantification of subsurface volumetric water content (VWC) remains a central challenge in hydrogeophysics, carrying direct implications for fields as diverse as precision agriculture, water resource management, and the forecasting of natural hazards such as flash floods and landslides. Cosmic Ray Neutron Sensing (CRNS) offers a non-invasive, field-scale approach that effectively bridges the significant resolution gap between highly localized point sensors and coarse-scale remote sensing. By monitoring the above-ground flux of low-energy cosmic ray neutrons, a signal inversely correlated with the total environmental hydrogen pool, CRNS integrates VWC over a representative elementary volume typically spanning tens of hectares. However, despite its operational elegance, the rigorous processing and reliable interpretation of the CRNS signal, particularly in complex, heterogeneous landscapes, necessitate methodological refinement. The fundamental ambiguity in interpretation arises from the complex spatial variability of soil moisture and lithology within the sensor's footprint, combined with the inherently nonlinear relationship between neutron count rate and VWC. This nonlinearity is known to result in a disproportionately stronger influence from drier soil regions, but the extent and modulation of this effect under realistic, spatially complex heterogeneity demand quantitative investigation.

This work presents a comprehensive, purely synthetic study designed to rigorously investigate the response of the CRNS detector system across a range of heterogeneous subsurface configurations. The overarching objective is to significantly advance the CRNS data processing and interpretation workflow by demonstrating the critical value of explicitly incorporating prior information derived from complementary geophysical characterization. Synthetic datasets were generated using the URANOS (Ultra Rapid Neutron-Only Simulation) Monte Carlo neutron transport code, which accurately simulates the complex neutron pathways through the atmosphere and the spatially variable subsurface. The methodology adopted an integrated approach, utilizing prior geophysical characterization, specifically Electrical Resistivity Tomography (ERT) and Electromagnetic Induction (EMI) inversion results, from the well-studied Borgo Grignanello (SI) field site in Italy. This characterization informed the creation of a realistic ground model featuring two main lithological units with distinct porosity and VWC ranges (Fig 1 bottom). The simulation suite (Fig. 1) included

two reference homogeneous cases, an idealized symmetric two-region domain, and both the realistic and an inverted spatial configuration of the geophysical model of the site, enabling the isolation and quantification of the influence of the CRNS detector's non-uniform spatial weighting function.

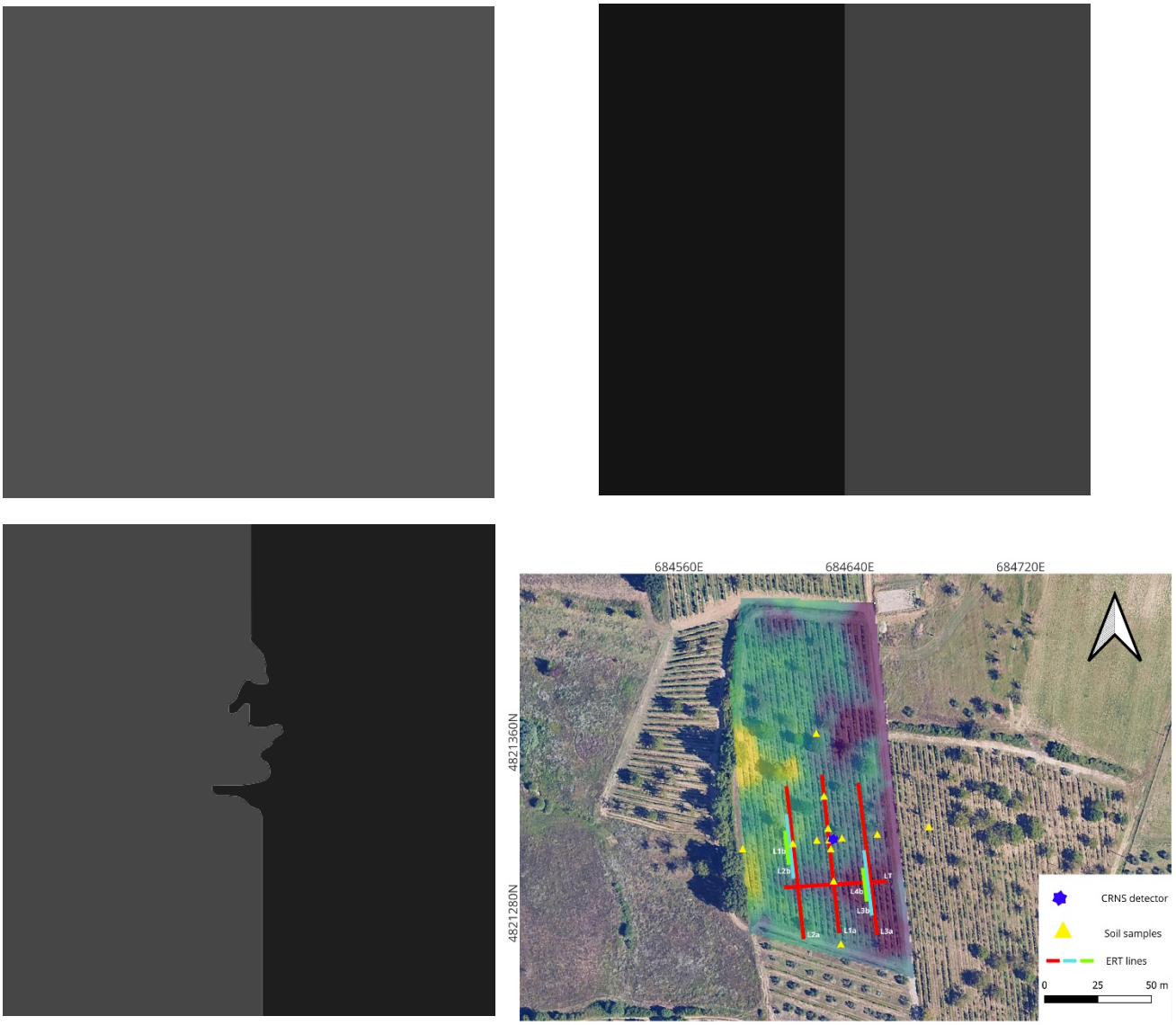

Figure 1 ***Top Left:*** *Example of homogeneous ground model as a png file image used in URANOS****. Top Right:*** *Representation of the idealized symmetric model****. Bottom Left:*** *Simplified map of the site heterogeneity of Borgo Grignanello.* ***Bottom Right:*** *Geophysical characterization setup and EMI map of the Borgo Grignanello site*

Neutron count rates obtained from URANOS were then converted into VWC time series using the open-source CoRNy software and the state-of-the-art Universal Transport Solution (UTS) forward model, ensuring a robust and physically consistent conversion across all simulated scenarios. The analysis of the resulting CRNS signals yielded crucial quantitative insights, confirming the hypothesis: for the heterogeneous configuration explicitly mimicking the complex conditions at Borgo Grignanello, the converted VWC derived from the CRNS signal was found to align remarkably (with a deviation of 1%) closely with the VWC value of the drier soil portion within the domain. This

result provides strong, site-specific synthetic confirmation of the predicted dry-region dominance effect. However, the study demonstrated that this relationship is not a universal constant but is critically modulated by the degree of non-homogeneity in VWC values, and the geometrical distribution of the heterogeneity: the precise position of the CRNS detector relative to the wet/dry interfaces, highlighting the complex, non-linear role of the detector's spatial weighting function.

The most critical outcome of this investigation lies in its methodological and practical utility for the hydrogeophysics community. The results unequivocally underscore and highlight the critical necessity of obtaining and integrating independent prior knowledge of subsurface heterogeneity for any robust and data-driven interpretation of CRNS time series. Since a simplistic interpretation of the CRNS signal as an unweighted spatial average can lead to significant errors, the fundamental utility of this research is the demonstration that the integration of CRNS with complementary geophysical methods, such as ERT and EMI for lithological and moisture-proxy mapping, is a necessary prerequisite for achieving a more conscious and reliable interpretation of the CRNS dataset. This multidisciplinary workflow enables the construction of a structurally and spatially informed conceptual model that, when incorporated into the CRNS data processing via tools like URANOS, moves the interpretation beyond a single, ambiguous VWC value toward a more nuanced and accurate assessment of the state of the heterogeneous soil moisture field. This integrated approach offers an immediate pathway toward reducing uncertainty in field-scale soil moisture assessments, supporting more efficient resource management, and enhancing the reliability of environmental monitoring in complex natural settings.

Acknowledgments

The authors gratefully acknowledge Dr. Markus Köhli and Dr. Jannis Weimar from the University of Heidelberg, Germany, for their invaluable theoretical guidance on the physics of cosmic-ray neutron sensing and for providing the necessary support with the specialized tools employed, including the URANOS Monte Carlo simulation code and CoRNy Software. Their expertise was essential for the successful completion and interpretation of this methodological study.

References

Köhli, M.; Schrön, M.; Zreda, M.; Schmidt, U.; Dietrich, P.; Zacharias, S.; 2015: Footprint characteristics revised for field-scale soil moisture monitoring with cosmic-ray neutrons. *Water Resources Research, Vol. 51, pp. 5772–5790,* https://doi.org/10.1002/2015WR017169

Köhli, M.; Schrön, M.; Zreda, M.; Schmidt, U.; Dietrich, P.; Zacharias, S.; 2015: Universal transport properties of cosmic-ray neutrons in the atmosphere near the ground. *Water Resources Research, Vol. 51, pp. 1141–1151,* https://doi.org/10.1002/2014WR016466

Köhli, M.; Weimar, J.; Schrön, M.; Baatz, R.; Schmidt, U.; 2021: Soil moisture and air humidity dependence of the above-ground cosmic-ray neutron intensity. *Frontiers in Water, Vol. 2, 544847,* https://doi.org/10.3389/frwa.2020.544847

Schrön, M.; Köhli, M.; Bogena, H. R.; Zacharias, S.; Vereecken, H.; 2017: The role of lateral transport for cosmic-ray neutron sensing in heterogeneous landscapes. *Journal of Hydrology, Vol. 540, pp. 923–933,* https://doi.org/10.1016/j.jhydrol.2016.07.039

Weimar, J. O.; 2022: Advances in cosmic-ray neutron sensing by monte carlo simulations and neutron detector development. *Doctoral dissertation.*

Zreda, M.; Desilets, D.; Ferré, T. P. A.; Scott, R. L.; 2012: Measuring soil moisture content non-invasively at intermediate spatial scale using cosmic-ray neutrons. *Geophysical Research Letters, Vol. 39, No. 2, L02402,* https://doi.org/10.1029/2011GL050016

Corresponding author: viola.cioffi@phd.unipd.it

EEMstudio & EEMverter LITE – Freeware/ opensource tools for processing and modelling Electrical & Electromagnetic data

G. Fiandaca[1,2], N. Sullivan[2], S. Galli[2]

[1] *The EEM Team for Hydro & eXploration, Dept. of Earth Sciences Ardito Desio, University of Milano, Italy*

[2] *The EEM Team Spin-Off company, Italy*

EEMstudio & EEMverter LITE

EEMstudio & EEMverter LITE are a Graphical User Interface (GUI) and Modelling Kernel for processing and modelling of Electrical (E) and Electromagnetic (EM) data distributed starting from November 2025 with Opensource (EEMstudio) and Freeware (EEMverter) licenses by the EEM Team Spin-Off company (www.the-eem-team.it), a spin-off of the University of Milano.

EEMverter (Fiandaca et al., 2024) has born with the intention of handling natively joint inversion of different data types (e.g. Chen et al., 2026 and Fiandaca et al., 2025 for 2D galvanic and 3D EM joint inversion; Signora et al., 2025b for 2D galvanic and 1D EM joint inversion), time-lapse inversion (e.g. Signora et al., 2025 for Airborne EM data; Ciraula et al., 2025 for galvanic data), induced polarization and all dimensionalities (1D,2D & 3D) in the forward response (e.g. Chen at al., 2025 for 3D Airborne EM modelling with IP (AIP); Dauti et al. 2026 and Dauti et al. 2025 for 1D AIP modelling; Ciraula et al. 2025 and Römhild et al., 2024 for galvanic full-decay IP modelling).

EEMverter key features are:

- Definition of distinct meshes for model parameter definition, forward computation and constraint definition (Madsen et al., 2020; Zhang et al., 2022) in vtk format, for being easily visualizable in Paraview (Ahrens et al., 2005).
- Parametric definition of electrical properties, such that the (complex) electrical conductivity is computed through functions, also integrating petrophysical relations (e.g. Römhild et al., 2024 for direct inversion of DCIP data in terms of hydraulic conductivity).
- Flexible definition of the inversion objective function, such as the data misfit, roughness misfit & prior misfit can be computed with the use of different norms, such as L1, L2, generalized Minimum (Gradient) Support (Fiandaca et al., 2015).
- Iterative inversion splitable in several inversion cycles, where inversion model and parameters, data and constraints are selected for producing comprehensive results.

EEMstudio (Sullivan et al., 2024) is a versatile QGIS plugin designed for processing, modelling, and inverting electrical and electromagnetic data.

EEMstudio key Features are:

- QGIS integration for intuitive geospatial analysis
- Specialized processing tools for electric and electromagnetic data in time domain
- Advanced modelling and inversion, powered by the EEMverter kernel
- Comprehensive visualization tools for geophysical data and results
- Open-source flexibility allowing community contributions and custom enhancements

Supported data types and formats

EEMstudio and EEMverter handle galvanic data with induced polarization, both in full-decay and integral chargeability, and TEM inductive data, with single soundings and ground-based acquisitions in continuous mode. EEMstudio features a built-in file converter, making it easy to convert data to the file format used in EEMstudio and EEMverter. The converters available in the LITE version are:

- Galvanic data – ABEM Terrameter .txt format (file exported directly from the Terrameter LS Toolbox); IRIS .bin format (native binary file format exported from the IRIS instruments); Res2DInv .dat format (resistivity-only and integral chargeability both supported with standard format); Generic .tx2 format (output of the full waveform processing tools developed at Aarhus/Lund University, Olsson et al., 2016);
- Inductive data – Loupe .dat format (Native export format from the Loupe instrument); tTEM .xyz/.lin format (file exported with TEM Data Manager software distributed by TEMcompany); TEM2Go .xyz/.lin format (file exported with TEM Data Manager software distributed by TEMcompany); sTEM .usf format (file exported with TEM Data Manager software distributed by TEMcompany); single sounding .usf format. with stacked data (e.g. SPIA export) and with raw data with multiple sweeps (e.g. WalkTEM export).

In the official release, both galvanic and inductive demo files are distributed, to allow the users easily accessible training datasets.

Available modelling of E & EM data in LITE versions

EEMstudio and EEMverter LITE allows several options for modelling of Direct Current (DC) and time-domain IP galvanic data and transient EM (TEM) data, both for single datasets and in time-lapse inversion.

Available galvanic modelling:

- Full-decay IP modelling, taking into account the current waveform and the system transfer function following Fiandaca et al. (2013), for 50% and 100% duty cycles (Olsson et al., 2025);

- Integral chargeability modelling, always considering the current waveform and the system transfer function for quantitative interpretation (Olsson et al., 2019).

Similarly to Fiandaca et al. (2013), the galvanic forward/jacobian computations are carried out in frequency domain, solving Poisson's equation in 2D with the finite element method, and time-transformed in time domain through the Hankel transform. Constant Phase Angle and Cole-Cole modelling are allowed for IP data, also with Maximum Phase Angle (MPA) re-parameterization (Fiandaca et al., 2018).

On the contrary, EM modelling in the LITE EEMverter version is carried out in 1D, following Effersø et al. (1999) and Sullivan et al. (2023), and modelling the current waveform with the Fitterman and Anderson (1987) approach. The available modelling for inductive data in EEMstudio/EEMverter LITE are:

- Single sounding TEM data, in both X and Z components and support for multiple moments and modelling of the transmitter shape;
- Ground-based multi-sounding TEM data in continuous acquisition, with both 2D and 3D inversion meshes with horizontal constraints.

No IP modelling nor airborne modelling Are supported in the LITE versions for inductive data, as well 3D computations.

Figure 1 presents and example of full-decay MPA inversion of galvanic data, while Figure 2 presents the inversion of tTEM inductive data along the same line.

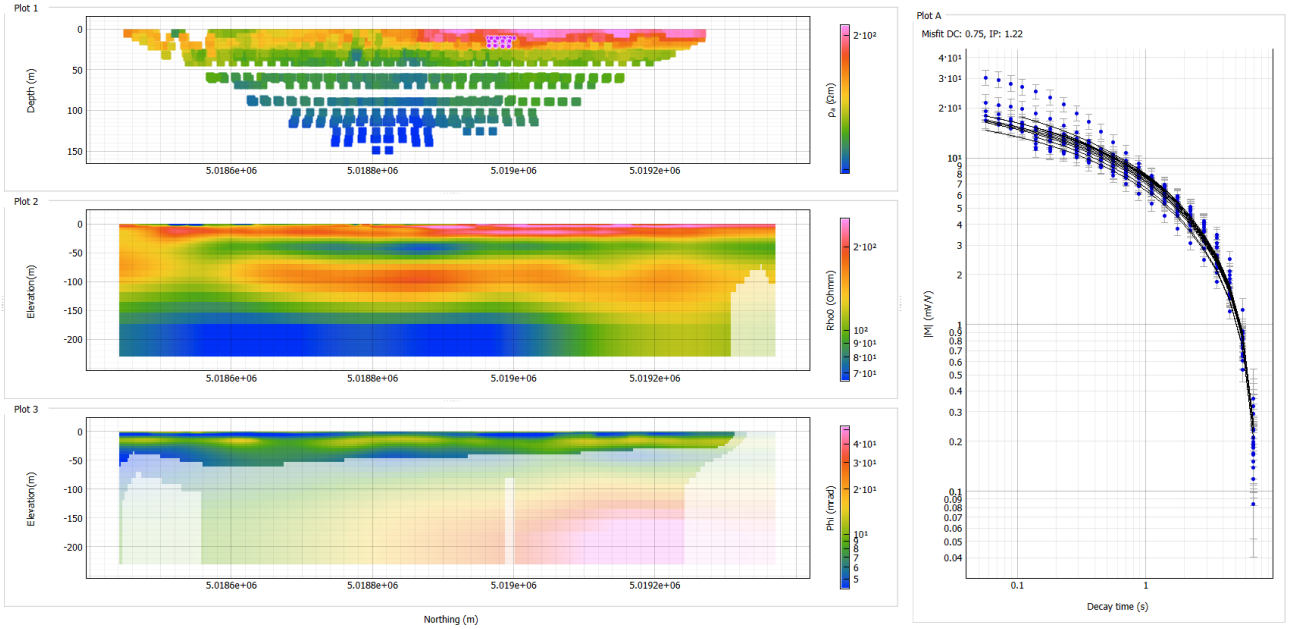

Fig. 1 – Direct current and full-decay Induced Polarization (DCIP) spectral inversion of galvanic data (Bubbiano demo file inverted with EEMverter and distributed with the EEMstudio/EEMverter LITE bundle) in terms of Maximum Phase Angle (MPA) Cole-Cole re-parameterization. Plots extracted from the Visualization App of EEMstudio. Plot 1: pseudosection of data. Plot 2: resistivity inversion section. Plot 3: chargeability (maximum phase) inversion section. Plot A: example of IP data fit (blue markers – data; black lines – forward). Depth of investigation in the inversion sections is shown with shading.

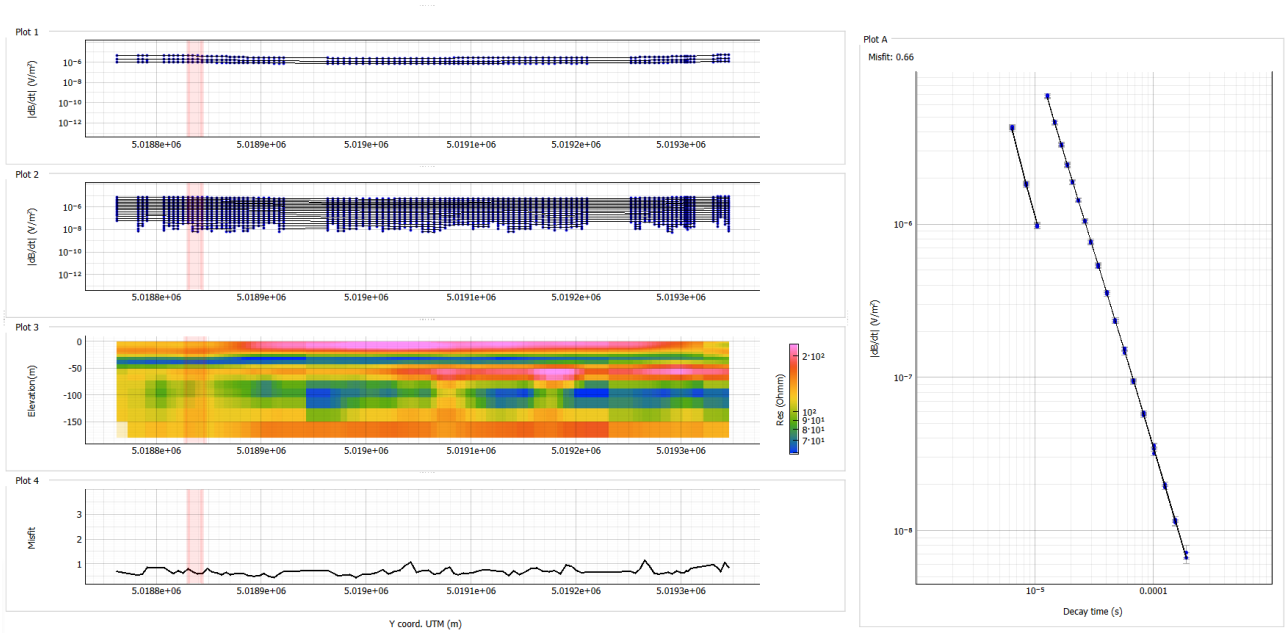

Fig. 2 – Inversion of tTEM inductive data of the Bubbiano demo file. Plots extracted from the Visualization App of EEMstudio. Plot 1: Low Moment data stripe (blue markers – data; black lines – forward). Plot 2: high Moment data stripe (blue markers – data; black lines – forward). Plot 3: resistivity inversion section. Plot 3: data misfit along the profile. Plot A: example of TEM soundings and fit (blue markers – data; black lines – forward). Depth of investigation in the inversion sections is shown with shading.

Workflows

Fig. 3 presents the workflow in EEMstudio/EEMverter for processing and inversion of data (Inversion Scheme) and modelling of synthetic data (Forward Scheme).

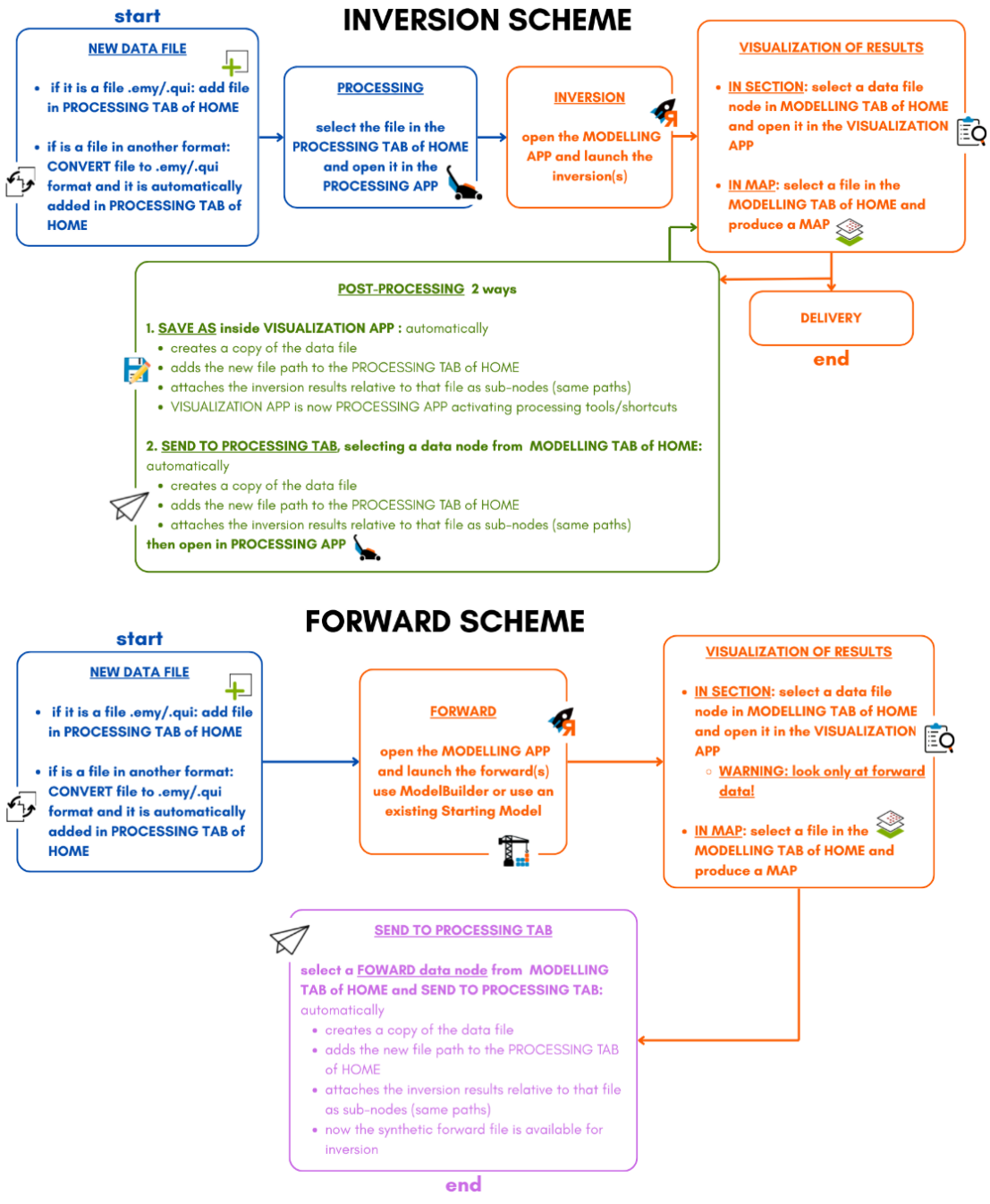

Fig. 3 – EEMstudio/EEMverter inversion and forward schemes. Inversion scheme: 1) data load or conversions; 2) processing of E & EM data, for culling outliers out in the QGIS environment, through the Processing App; 3) data inversion with Modelling App; 4) visualization of inversion results and data fit; 5) delivery or post-processing for improving the processing with the help of the inversion results. Forward scheme: 1) selection of data; 2) forward modelling through Modelling App; 3) visualization of modelling results through Visualization App; 4) inversion of synthetic data.

Conclusions

We presented EEMstudio and EEMverter LITE, a novel processing and modelling environment for electrical and electromagnetic data with focus on induced polarization distributed with Opensource (EEMstudio) and Freeware (EEMverter) licenses. The LITE version of the software allows to process and model: 1) DC and integral chargeability/full-decay IP data in 2D; 2) TEM data in stationary and continuous acquisition modes, such as tTEM, Tem2Go, sTEM and Loupe; 3) time-lapse data, both galvanic and inductive. We believe that EEMstudio and EEMverter LITE, with their common processing and modelling environment for galvanic and inductive data integrated in QGIS, will advance the usability of Electrical and Environmental methods for both researchers and practitioners.

References

Ahrens, J., Geveci, B., & Law, C. (2005). ParaView: An End-User Tool for Large Data Visualization. In *Visualization Handbook*. Elsevier.

Chen, J., Dauti, Fiandaca, G. (2026). Joint inversion of inductive and galvanic data: significant resolution improvement honouring both data types – 3D EM and 2D DCIP. In *Book of Abstracts 4tth National Conference, GNGTS 2026, Udine, Italy, 2026* (pp. 1-6).

Chen, J., Dauti, F., Wertich, V., Viezzoli, A., Zhang, B., & Fiandaca, G. (2025). 3-D EM inversion considering induced polarization effect. *Geophysical Journal International*, *244*(1), ggaf462, in press.

Ciraula, D.A., Fiandaca, G., Chen, J., Scott, S., Lévy, L. (2025) Constraining Time-lapse Geophysical Responses with Reactive Transport Modeling: An Approach to Monitor H_2S Mineral Storage. *Geophysical Journal International*, in press.

Dauti, F., Munday, T., Mulè, S., Viezzoli, A., Fiandaca, G. (2026). Induced Polarization effects in airborne EM systems: fixed-wing and helicopter-borne measurements. In *Book of Abstracts 4tth National Conference, GNGTS 2026, Udine, Italy, 2026* (pp. 1-7).

Dauti, F., Ley Cooper, Y., Munday, T., Viezzoli, A., Fiandaca, G. (2025). Induced polarization effects in fixed-wing airborne EM: the TEMPEST^{TM} system – Part A, connecting numerical modelling with field evidence at continental scale, *Geophysical Journal International*, ggaf495, in press.

Effersø, F., Auken, E., & Sørensen, K. I. (1999). Inversion of band-limited TEM responses. *Geophysical Prospecting*, 47(4), 551-564.

Fiandaca, G., Chen, J., Signora, A., & Dauti, F. (2025). Joint inversion of Electrical and Electromagnetic data–Part II: Induced Polarization and 3D EM modelling. In *NSG 2025: 6th Conference on Geophysics for Mineral Exploration and Mining* (Vol. 2025, No. 1, pp. 1-5). European Association of Geoscientists & Engineers.

Fiandaca, G., Chen, J., & Zhang, B. (2024). EEMverter, a new modelling tool for Electric and Electromagnetic data with focus on induced polarization. In *NSG 2024 30th European Meeting of Environmental and Engineering Geophysics* (Vol. 2024, No. 1, pp. 1-5). European Association of Geoscientists & Engineers.

Fiandaca G., Meldgaard Madsen L., Maurya P.K. (2018). Re-parameterisations of the Cole-Cole model for improved spectral inversion of induced polarization data, *Near Surface Geophysics*, 16 (4), 385-399. https://doi.org/10.3997/1873-0604.2017065

Fiandaca G., Doetsch J., Vignoli G. & Auken E. (2015). Generalized focusing of time-lapse changes with applications to direct current and time-domain induced polarization inversions, *Geophysical Journal International,* 203, 1101-1112. https://doi.org/10.1093/gji/ggv350

Fiandaca G., Ramm J., Binley A., Gazoty A., Christiansen A.V. & Auken E. (2013). Resolving spectral information from time domain induced polarization data through 2-D inversion, *Geophysical Journal International,* 192, 631-646. https://doi.org/10.1093/gji/ggs060

Fitterman, D. V., & Anderson, W. L. (1987). Effect of transmitter turn-off time on transient soundings. *Geoexploration*, *24*(2), 131-146.

Madsen, L. M., Fiandaca, G., & Auken, E. (2020). 3-D time-domain spectral inversion of resistivity and full-decay induced polarization data—full solution of Poisson's equation and modelling of the current waveform. *Geophysical Journal International*, *223*(3), 2101-2116. https://doi.org/10.1093/gji/ggaa443

Olsson, P. I., Fiandaca, G., Maurya, P. K., Dahlin, T., & Auken, E. (2019). Effect of current pulse duration in recovering quantitative induced polarization models from time-domain full-response and integral chargeability data. *Geophysical Journal International*, *218*(3), 1739-1747. https://doi.org/10.1093/gji/ggz236

Olsson P.-I., Fiandaca G., Larsen J.J., Dahlin T. & Auken E. (2016). Doubling the spectrum of time-domain induced polarization by harmonic de-noising, drift correction, spike removal, tapered gating and data uncertainty estimation, *Geophysical Journal International,* 207 (2), 774-784. https://doi.org/10.1093/gji/ggw260

Olsson P.-I., Dahlin T., Fiandaca G. & Auken E. (2015). Measuring time-domain spectral induced polarization in the on-time: decreasing acquisition time and increasing signal-to-noise ratio, *Journal of Applied Geophysics,* 123, 316-321. https://doi.org/10.1016/j.jappgeo.2015.08.009

Römhild, L., Fiandaca, G., Bayer, P. (2024). Joint inversion of induced polarization and hydraulic tomography data for hydraulic conductivity imaging. *Geophysical Journal International*, Volume 238, Issue 2, August 2024, Pages 960–973, https://doi.org/10.1093/gji/ggae197

QGIS.org, 2025. QGIS Geographic Information System. QGIS Association. http://www.qgis.org.

Signora, A., Munday, T., Vonk, M. A., & Fiandaca, G. (2025). Time-Lapse Airborne EM for monitoring the evolution of a saltwater aquifer-The Bookpurnong case study. *Geophysical Journal International*, *244*(1), ggaf414, in press.

Signora, A., Galli, S., Dauti, F., Chen, J., Munday, T., & Fiandaca, G. (2025b). Joint inversion of Electrical and Electromagnetic data–Part I: unprecedented resolution improvements. In *NSG 2025: 31st Meeting of Environmental and Engineering Geophysics* (Vol. 2025, No. 1, pp. 1-5). European Association of Geoscientists & Engineers.

Sullivan, N. A. L., Viezzoli, A., Fiandaca, G. (2024). EEMstudio: process and model electric and electromagnetic data with a QGIS plugin. In *NSG 2024 30th European Meeting of Environmental and Engineering Geophysics* (Vol. 2024, No. 1, pp. 1-5). European Association of Geoscientists & Engineers.

Sullivan, N.A.L., on behalf of Gisolo, M., Spagnoli, L., Rapiti, A., Dauti, F., Menghini, A., Viezzoli, A., Fiandaca, G. (2023). Airborne EM in northern Italy for sustainable and resilient management of groundwater resources. *Il Nuovo Cimento, 46(3), 68*. DOI: 10.1393/ncc/i2023-23068-y

Zhang, B., Engebretsen, K. W., Fiandaca, G., Cai, H., & Auken, E. (2021). 3D inversion of time-domain electromagnetic data using finite elements and a triple mesh formulation. *Geophysics*, *86*(3), E257-E267. https://doi.org/10.1190/geo2020-0079.1

Corresponding author: gianluca.fiandaca@unimi.it

Full Waveform Inversion by means of Implicit Neural Representation: Application to Field Data from a Geothermal Area

F. Macelloni[1], S. Berti[1], M. Aleardi[1], A. Tognarelli[1], E. Stucchi[1]
[1] *University of Pisa, Earth Sciences Department, Italy*

Introduction

One of the most powerful tools in seismic methods for subsurface imaging is represented by Full Waveform Inversion (FWI; Virieux and Operto, 2009). It consists of an optimization problem in which the difference between observed and modelled seismogram is iteratively minimized to estimate the velocity distribution of the investigated subsurface. The idea behind FWI is to employ the entire information content of the seismic data, considering both amplitude and phase. This leads to potential for high-resolution imaging, but it comes with its own challenges and limitations, due to the strong non-linearity and the ill-posedness of this inverse problem. Main issues when applying FWI are represented by the cycle-skipping and the reliance on the starting model. Indeed, a good initial model is crucial for the success of the approach, avoiding the optimization to get stuck in local minima of the objective function. Common strategies to cope with these challenges include the use of alternative misfit functions, enhancement of low frequencies in the data, the use of global optimization approaches or casting the inversion in a probabilistic framework to better explore the solution space.

In this work we use a machine learning approach, the Implicit Neural Representation (INR), to solve the FWI. We build a continuous representation of the velocity model, instead of a standard grid-based one, through the parameters of a simple Multi Layer Perceptron (MLP) and we optimize for them. Sun et al. (2023) demonstrated the effectiveness of this approach in seismic FWI and that it reduces the dependency on the initial model, being able to converge even when starting from a random initialization. Therefore, implicit representations can be regarded as an alternative reparameterization, able to preserve fine details and to reduce the computational complexity of a grid-based inversion. Its effectiveness partially depends on the frequency bias property of deep-learning optimization, namely the ability to learn and update from low to high frequency components.

We present here an application of INR FWI to field data from the CROP project, a large-scale Italian deep-crustal exploration program, deployed in the ‘80s and ‘90s. In particular, we consider a data extracted from the CROP-18A 2D seismic line dataset, acquired in southern Tuscany across the Larderello geothermal area to investigate the relationship between deep crustal structures and geothermal activity (Bertelli et al., 2003; Scrocca et al., 2003). Previous studies on the same seismic

line (de Franco et al., 2019; Tognarelli et al., 2020) can provide useful information to validate our results.

Methods

Unlike purely data-driven models, which often struggles to generalize beyond their training set, FWI is governed by physical equations describing wave propagation, ensuring predictive consistency and interpretability. This connection suggests that combining deep learning with the underlying physics of FWI can lead to more robust and generalizable inversion framework (Sun et al., 2023). Most of the deep-learning approaches to FWI inherit its traditional challenges, especially the strong reliance on initial model.

In the context of shape representation, coordinate-based Deep Neural Network are able to learn continuous functions (Sitzmann et al., 2020). Once trained, such networks can act as implicit representations of objects or scenes, enabling high-quality image or 3D surface reconstruction from the input coordinates. As explained in Sun et al. (2023), Deep Neural Representation models a continuous function that maps input coordinates to features of interest. After training, the network approximates the continuous function yielding a smooth and memory efficient representation. Compared to grid-based discretization, the INR stores information in a continuous form, preserving fine details without dependence on spatial resolution.

When applied to seismic inversion, INR can represent subsurface physical parameters $\mathbf{m}(\mathbf{x})$ within the constraints imposed by the wave equation. This leads to INR FWI, where the forward model $\mathcal{F}$ satisfies

$$\mathbf{R}\mathcal{F}(\mathbf{m}, s, \mathbf{x}, t) - \mathbf{d} = 0$$

with $\mathbf{R}$ denoting the matrix of receiver layouts, s the source, $\mathbf{x}$ the spatial coordinates, t the time and $\mathbf{d}$ the observed data. Replacing the model parameters $\mathbf{m}$ with the neural network $\mathcal{N}_\Theta(\mathbf{x})$, we obtain the formulation for the optimization problem of INR FWI:

$$\underset{\Theta}{\operatorname{argmin}} \|\mathbf{R}\mathcal{F}(\mathcal{N}_\Theta(\mathbf{x}), s, \mathbf{x}, t) - \mathbf{d}\|^2$$

with the network implicitly representing the velocity model.

We implement INR by considering a MLP, i.e. a network made of sequential layers of interconnected neurons, each performing a weighted sum of its inputs, followed by a nonlinear activation function. The output $a_i^{(l)}$ of the neuron i in layer l is computed as:

$$a_i^{(l)} = f\left(W_i^{(l)} a_i^{(l-1)} + b_i^{(l)}\right)$$

where $W_i^{(l)}$ and $b_i^{(l)}$ are the weight and the bias associated to the considered neuron and f represents the activation function.

To effectively capture high-frequency and spatially complex variations in the subsurface velocities, we adopt a sinusoidal representation network (SIREN), proposed by Sitzmann et al. (2020). This type

of INR employs periodic activation functions and, compared to other types of activations, can represent fine details and high-order derivatives more accurately. Thus, the output of a neuron becomes

$$a_i^{(l)} = \sin\left(\omega_0 W_i^{(l)} a_i^{(l-1)} + b_i^{(l)}\right)$$

with ω_0 representing a tunable parameter which affects the frequency that the network is able to capture.

To start the inversion from a given initial model, we need to train the network to represent it. Given a grid of spatial coordinates as input and the corresponding values of the velocity field as output, the training adapts the network parameters by minimizing the difference between ground truth and predicted velocities. We do not train the network, but we randomly initialize the weights, following what suggested in Sitzmann et al. (2020) and Sun et al. (2023). To do so, we randomly draw weights so that

$$W_i^{(l)} \sim \mathcal{U}\left(-\sqrt{6/n}, \sqrt{6/n}\right)$$

with $\mathcal{U}$ representing a uniform distribution and n the number of input features fed into the layer. This ensures that the input of each sinusoidal activation function is normally distributed with unitary standard deviation (Sitzmann et al. (2020)).

Results

The dataset considered in this work consists of 10 shots (explosive source) recorded by 192 geophones, deployed in an asymmetric split spread configuration, characterized by a maximum offset ranging between 6 km and 7.7 km. We considered the first 3 s of the recorded signal, with a sampling interval of 4 ms.

To compute the forward modelling, we discretize the domain in a grid with nz=42 nodes on the vertical and nx=1565 on the horizontal direction, respectively. The grid spacing is 30 m in both directions, thus the considered domain is about 1.2 km deep and extends horizontally for about 47 km. In our modelling, we did not include topography, thus we considered a datum at 200 m above sea level to refer the data, and we applied the static corrections for sources and receivers available in the dataset. The source signature has been estimated by selecting short offset traces, flattening the first arrival and stacking them to obtain a mean wavelet. The forward modelling code is Deepwave (Richardson, 2022), which employs finite-difference method to numerically solve the wave equation and automatic differentiation to compute gradients.

To prepare the data for the application of FWI and to enhance refracted and diving waves, on which we focus in our study, we applied a simple pre-processing consisting in a low-pass filter up to 10 Hz, top and bottom muting to select only the portion of seismogram of our interest and a trace-by-trace normalization. Fig.1(a) and Fig.1(b) show one of the considered shot gathers before and after the pre-processing, respectively. Instead, Fig.1(c) shows the position along the line of sources and receivers for the 10 shots considered, with the extension of the inverted model.

To implement the INR FWI, we consider a MLP with two hidden layers of 32 neurons each, for a total number of 2241 network parameters and sinusoidal activation functions. Note that these are the unknowns of the inversion and by representing the model through the MLP, the number of parameters is substantially reduced with respect to a standard grid-based inversion, which would involve nx·nz=65730 unknowns for the same spatial discretization used in the forward modelling. The frequency ω_0 for the SIREN is set to 10. For the optimization, we run the FWI for 6000 iterations, using the Adam optimizer. The selection of architecture and tunable hyperparameters comes from experience made on synthetic tests and trial and error procedure to understand the configuration that works better in our field data application. The inversion procedure took about 6 hours on a server equipped with Intel® Xeon® Silver 4114 CPU @2.20 GHz. This time is considerably reduced when using GPUs.

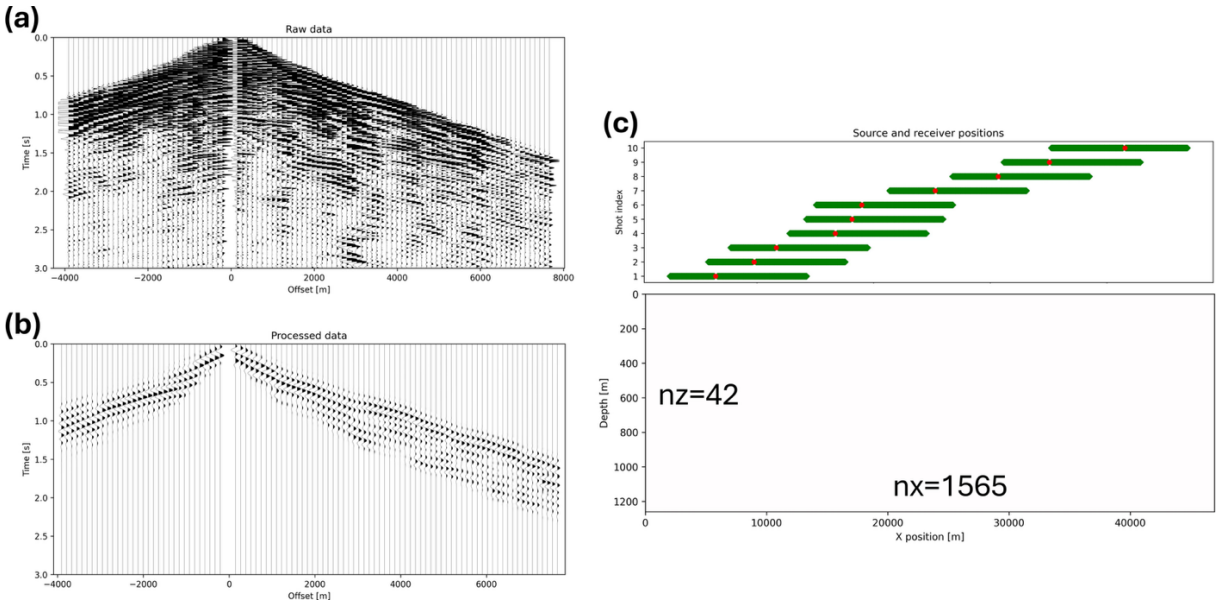

Fig. 1 – One shot gather before (a) and after (b) the pre-processing steps. (c) Positions along the horizontal axis of the sources (in red) and the receivers (in green) for the different shots, with the extension of the inverted model, expressed both in meters and in grid points.

To test the robustness of the INR FWI against initialization, we decided to run the inversion starting from a random model, obtained with a random initialization of the network weights and biases as previously discussed. The random initial model is represented in Fig.2(a), whilst Fig.2(b) shows the model predicted after the inversion. Focusing on the most illuminated portion, thus excluding the less reliable lateral and bottom edges of the domain, we note the left portion of the model shows high velocities at shallow depth or at surface, whilst the right side is characterized by lower velocities, pertaining to a sedimentary basin. This prediction is consistent with the results shown in Tognarelli et al. (2020). As stated in that study, the alternation of higher and lower velocities at surface level corresponds to the sequence of the outcropping hard and soft formations. Velocities of 5-6 km/s can be associated to metamorphic formations, whilst the increment up to about 7 km/s could be due to the presence of intrusive bodies (Tognarelli et al., 2020).

To better understand the reliability of the result obtained with INR FWI, we check the data fitting. Fig.3(a) shows the comparison of the observed data (black) and the initial data (red). The observed

data is then compared for the same shot gather to the data computed on the predicted model (Fig.3(b)). We note an improvement in the fitting of the first events, with the INR FWI that was able to partially solve the highly cycle-skipped initial data. This is supported by the close-ups on some traces shown in Fig.3(c). The phase of the first three or four observed cycles is well reproduced in the prediction, with some mismatch in the amplitudes, even when the initial data was completely missing those events.

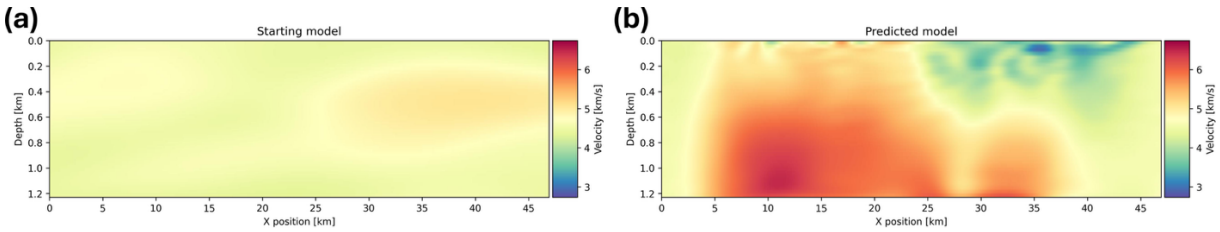

Fig. 2 – The random starting model (a) and the model predicted by INR FWI (b).

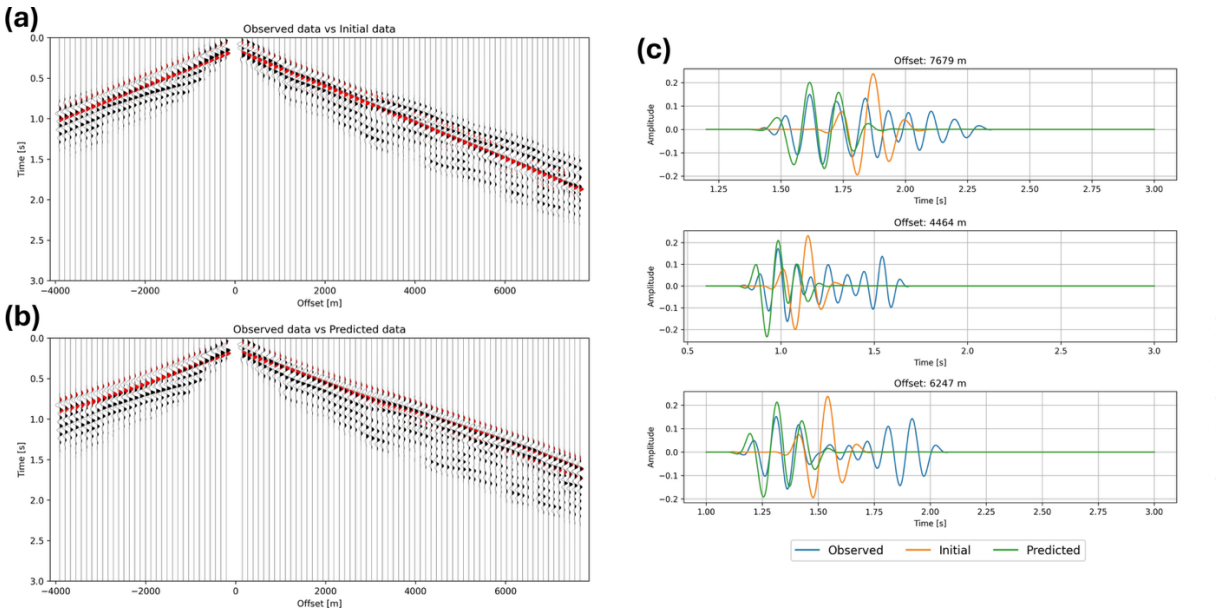

Fig. 3 – Comparison of observed (black) and data computed (red) on the starting model (a) and on the final FWI predicted model (b). Close-ups of some traces (c).

Conclusions

In this study we tested the INR FWI proposed in Sitzmann et al. (2020) and Sun et al. (2023) on field data from a geothermal area. The predicted model is consistent with the results reported in Tognarelli et al. (2020) on the same CROP-18A seismic line.

The INR FWI offers a promising alternative to standard FWI implementations. The model representation through the network parameters and the frequency bias property lead to inherent regularization of the solution and to alleviate the necessity of an informative and accurate initial model. Indeed, the method, as shown in this study, is able to converge to reliable and meaningful solutions even when starting from a random initial guess.

Further improvements could come from extending the analysed dataset by including more shots in the inversion and taking into account the topography in the modelling.

References

Bertelli L., Mazzotti A., Persoglia S.; 2003: Planning, acquisition and processing of the CROP seismic data. Memorie Descrittive Carta Geologica d'Italia, pp. 47-54.

de Franco R., Petracchini L., Scrocca D., Caielli G., Montegrossi G., Santilano A., Manzella A.; 2019: Synthetic Seismic Reflection Modelling in a Supercritical Geothermal System: An Image of the K-Horizon in the Larderello Field (Italy). Geofluids, 8492453. https://doi.org/10.1155/2019/8492453.

Richardson A.; 2022: Deepwave. https://ausargeo.com/deepwave/ .

Scrocca D.; 2003: CROP Atlas: seismic reflection profiles of the Italian crust. Istituto Poligrafico e Zecca dello Stato.

Sitzmann V., Martel J., Bergman A., Lindell D., Wetzstein G.; 2020: Implicit neural representations with periodic activation functions. Advances in Neural Information Processing Systems, 33.

Sun J., Innanen K., Zjang T., Trad D.; 2023: Implicit seismic full waveform inversion with deep neural representation. Journal of Geophysical Research: Solid Earth, 128, e2022JB025964. https://doi.org/10.1029/2022JB025964.

Tognarelli A., Stucchi E., Mazzotti A.; 2020: Velocity model estimation by means of Full Waveform Inversion of transmitted waves: An example from a seismic profile in the geothermal areas of Southern Tuscany, Italy. Geothermics, 88, 101894. ISSN 0375-6505. https://doi.org/10.1016/j.geothermics.2020.101894.

Virieux J., Operto S.; 2009: An overview of full-waveform inversion in exploration geophysics. Geophysics, 74, no. 6, WCC1-WCC26.

Corresponding author: Fabio Macelloni, fabio.macelloni@phd.unipi.it

ADERT: Automatic differentiation-based electrical resistivity tomography

F. Rincón[1], M. Aleardi[1], E. Cuellar[2], S. Berti[1], A. Tognarelli[1], E. Stucchi[1]
[1] *University of Pisa, Italy*
[2] *Independent researcher*

Introduction

Electrical resistivity tomography (ERT) is a widely applied geophysical imaging technique for resolving subsurface resistivity variations, with applications ranging from hydrogeology and environmental studies to engineering and geohazard assessment. Conventional ERT inversion strategies are typically deterministic and rely on smoothness-constrained formulations, which provide stable solutions and rapid convergence but offer limited insight into model uncertainty. This limitation is particularly relevant in complex geological environments, where non-uniqueness and uneven data sensitivity may strongly affect interpretation.

Both deterministic and probabilistic inversion methods critically depend on the accurate and efficient computation of gradients of the objective function with respect to model parameters. Classical approaches for gradient computation include finite-difference (FD) approximations and Jacobian–vector (JV) or adjoint-based methods. Although Jacobian–vector products can in principle be extended to alternative parameterisations through the chain rule, doing so requires manual derivation and implementation of dense mappings, making the approach considerably less flexible and efficient than automatic differentiation, which supports such transformations natively.

Recent advances in machine learning have promoted the widespread use of automatic differentiation (AD) as a general and exact tool for gradient computation. AD enables machine-precision derivatives through arbitrary sequences of differentiable operations, eliminating the need for explicit Jacobian construction or adjoint derivations. Despite its success in seismic and other geophysical inverse problems, the application of AD to ERT inversion—particularly in probabilistic frameworks and reduced-order parameterisations—remains largely unexplored. In this work, we introduce ADERT, a fully differentiable framework for electrical resistivity tomography inversion based on automatic differentiation. ADERT reimplements the ERT forward modelling engine within the PyTorch ecosystem, allowing gradients to be computed seamlessly through the entire modelling pipeline. We validate the accuracy and efficiency of AD-based gradients against classical FD and JV approaches, and we demonstrate the flexibility of the framework through deterministic and probabilistic inversions. Special emphasis is placed on a field-data application, where ADERT enables efficient uncertainty quantification using a probabilistic inversion in a compressed model space.

Methods

ADERT is built around a forward modelling engine that reproduces the finite-volume discretisation commonly adopted in ERT but implemented entirely using PyTorch tensors. This design ensures that all computational steps—including conductivity transformation, system matrix assembly, solution of the Poisson equation, and data projection—are embedded within a differentiable computational graph. As a result, simulated data are fully differentiable with respect to the resistivity model, enabling exact gradient computation via reverse-mode automatic differentiation. From a theoretical perspective, the forward operator $\mathcal{F}$ can be expressed as a composition of elementary differentiable operations acting on the model parameters. Automatic differentiation evaluates the total derivative of $\mathcal{F}$ with respect to the model $\mathbf{m}$ by recursively applying the chain rule through all intermediate variables, such that:

$$\frac{\partial \mathcal{F}}{\partial \mathbf{m}} = \frac{\partial v_k}{\partial v_{k-1}} \cdot \frac{\partial v_{k-1}}{\partial v_{k-2}} \cdot \frac{\partial v_1}{\partial \mathbf{m}}.$$

This recursive application of the chain rule propagates derivatives from $\mathbf{m}$ through all intermediate computations $v_i = f_i(v_j, v_k, \dots)$. In this way, ADERT computes exact gradients efficiently and at machine precision, without requiring manual derivation or explicit Jacobian storage. The resulting gradients are both accurate and computationally efficient, thanks to reverse-mode accumulation. Unlike symbolic or numerical differentiation, automatic differentiation operates directly on the computational graph, supports dynamic control flow, and avoids approximation errors, making it particularly well suited for large-scale, differentiable physics-based simulations.

To assess the accuracy of AD-based gradients, we compare them against two benchmark methods: finite-difference approximations of the Jacobian and the Jacobian–vector (JV) approach implemented in the SimPEG framework. Finite differences provide a straightforward reference but are computationally expensive and sensitive to perturbation size. The JV method efficiently computes gradients without storing the full Jacobian, but relies on manually derived sensitivity expressions tied to the full-domain discretisation. All gradients are evaluated with respect to the same least-squares objective function to ensure a fair comparison. Beyond deterministic inversion, ADERT supports probabilistic inference through gradient-based variational methods. In the deterministic setting, we solve the ERT inverse problem using a smoothness-constrained formulation optimized with the L-BFGS-B algorithm, where gradients of the objective function are computed exactly via automatic differentiation. This approach provides fast convergence and stable solutions while serving as a reference model for subsequent uncertainty analysis. For probabilistic inversion, we adopt Annealed Stein Variational Gradient Descent (A-SVGD), a particle-based variational inference method that approximates the posterior distribution by iteratively transporting an ensemble of particles toward regions of high posterior probability (D'Angelo & Fortuin, 2021; Corrales et al., 2025; Berti et al., 2025). The algorithm incorporates an annealing schedule that dynamically balances repulsive and attractive interactions between particles, enabling broad exploration of the model space during early iterations and progressive convergence toward dominant posterior modes at later stages. Here again, the gradients required by A-SVGD are efficiently computed via AD, allowing efficient probabilistic inversion even when operating in reduced or transformed parameter spaces.

To reduce computational cost and mitigate ill-conditioning, we adopt a Discrete Cosine Transform (DCT) parameterisation of the resistivity model for the probabilistic inversion (Aleardi et al., 2021,

Rincón et al., 2025). Only a subset of low-frequency DCT coefficients is retained, significantly reducing the number of unknowns. Unlike classical approaches—where gradients in the compressed domain would require finite differences or manual chain-rule derivations—ADERT allows gradients to be back-propagated directly from the data to the retained DCT coefficients, with no additional implementation effort.

Results

Gradient comparison: To evaluate the accuracy and efficiency of the AD-based gradients implemented in ADERT, we first compare them against FD and JV gradients for a synthetic ERT benchmark. Figure 1 illustrates the spatial distribution of the gradients computed using the three approaches for the same reference model and objective function. All gradients exhibit consistent sensitivity patterns, with the highest amplitudes concentrated beneath the electrode array and around the target anomaly. Minor discrepancies are limited to shallow regions where the problem is strongly non-linear. From a computational perspective, the AD-based gradient achieves a substantial speedup relative to FD approximations and comparable or improved performance with respect to the JV method, particularly when executed on GPUs. These results demonstrate that automatic differentiation provides both numerical accuracy and computational efficiency, validating its use as a reliable alternative to traditional sensitivity-based approaches for ERT inversion.

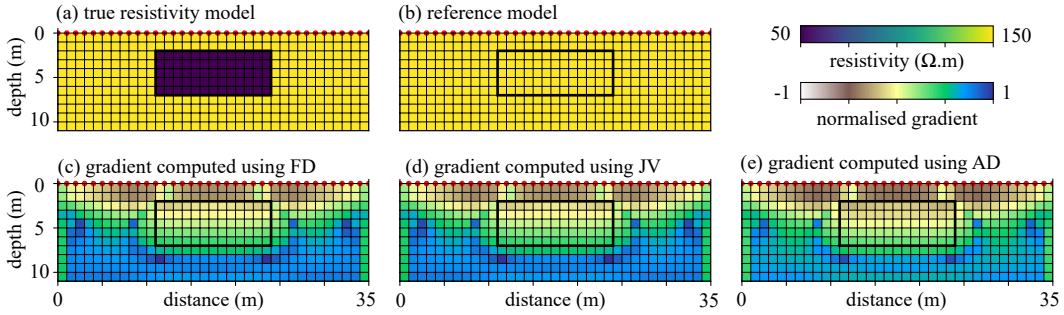

Fig. 1 – Spatial distribution of gradients computed using (a) finite differences, (b) the Jacobian–vector method, and (c) automatic differentiation for a synthetic resistivity model. The three approaches exhibit consistent sensitivity patterns, confirming the accuracy of AD-based gradients.

Field data application: Now we show the performance of ADERT using a field dataset acquired along a 208 m-long profile over a landslide-prone area. The dataset consists of 198 apparent resistivity measurements collected with 8 m electrode spacing, with the primary objective of delineating subsurface resistivity contrasts potentially associated with the landslide rupture surface. A deterministic inversion using AD-based gradients converges rapidly from a homogeneous starting model and achieves a strong reduction in data misfit. The recovered resistivity image reveals a shallow conductive layer overlying a more resistive domain at depth, consistent with previous geological interpretations of the site (see Figure 2).

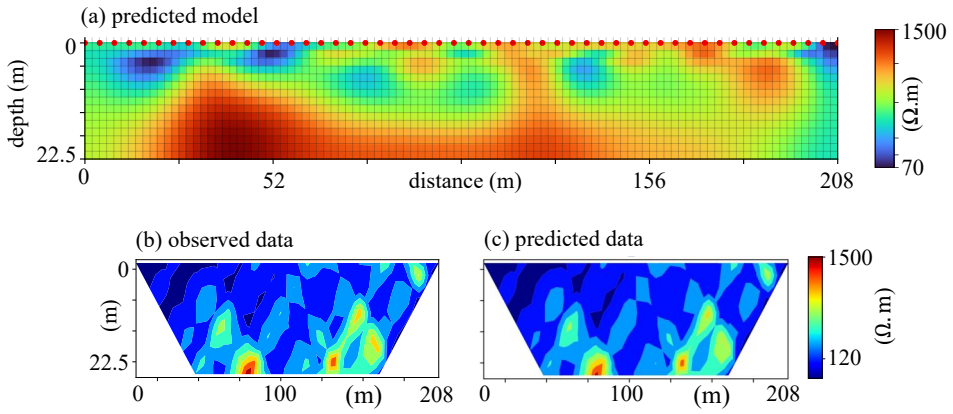

Fig. 2 – Results from the deterministic inversion using ADERT. (a) Predicted resistivity model showing near-surface conductive features and deeper resistive structures. (b) Observed and (c) predicted apparent resistivity pseudosections. The inversion converged to a final normalised misfit of 5.3 %.

We then perform a probabilistic inversion using the Annealed Stein Variational Gradient Descent (A-SVGD) algorithm in a DCT-compressed model space. In the following experiment, we assess inversion performance using 300 particles and 500 iterations. The prior assumptions are illustrated in Figure 3, where the prior mean corresponds to a homogeneous model of 800 Ω.m. Figure 3b shows two prior realisations drawn from a Gaussian distribution with exponential correlograms describing horizontal and vertical spatial correlations.

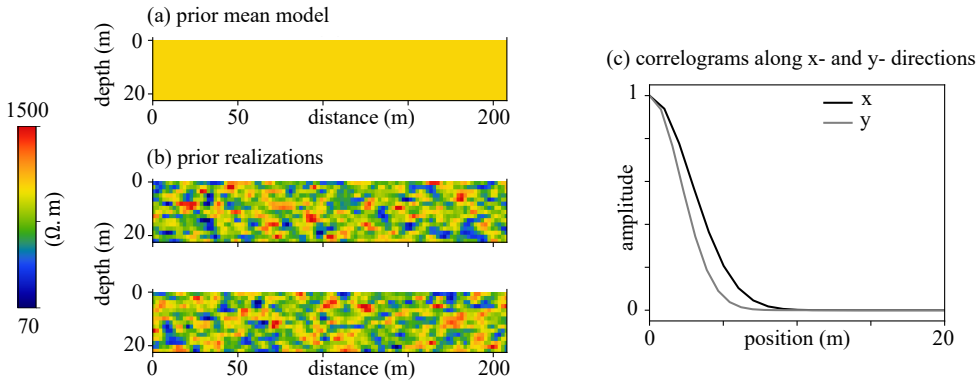

Fig. 3 – (a) Prior mean resistivity model. (b) Two random prior realisations sampled from the Gaussian covariance function. (c) Exponential correlograms along the horizontal (x) and vertical (y) directions, used to construct the prior covariance.

Following Rincón et al. (2025), who inverted the same field dataset, we retained 10×30 coefficients along the horizontal (x) and vertical (y) directions, preserving 99 % signal information while achieving significant compression. Figure 4 shows the posterior mean resistivity model and the corresponding posterior standard deviation obtained from the final ensemble of particles. The posterior mean closely resembles the deterministic solution but displays sharper resistivity contrasts and improved delineation of subsurface features. The posterior standard deviation highlights zones of increased uncertainty at depth and near the lateral boundaries, where data

sensitivity is reduced. Uncertainty systematically increases with depth, reaching several hundred Ω·m in poorly constrained regions. By incorporating AD and DCT into the probabilistic approach, the overall computational cost is reduced by more than 50 % compared to a full-domain AD implementation, making uncertainty quantification feasible for realistic ERT field datasets.

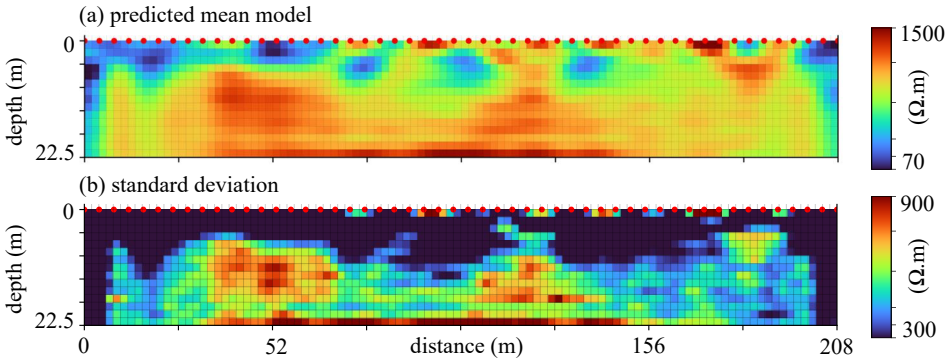

Fig. 4 – Results from the probabilistic inversion using ASVGD. (a) Posterior mean resistivity model obtained by averaging all particles at the final iteration. (b) Posterior standard deviation quantifying the uncertainty of the estimated resistivities.

Conclusion

This work introduces ADERT, a fully differentiable framework for electrical resistivity tomography inversion that leverages automatic differentiation to compute exact gradients through the entire forward modelling pipeline. Gradient comparisons confirm that AD-based derivatives are consistent with classical finite-difference and Jacobian–vector approaches, while offering superior flexibility and competitive computational performance. The field-data application demonstrates that ADERT enables robust deterministic inversion and efficient probabilistic inversion with meaningful uncertainty quantification. By allowing gradients to be computed directly in compressed parameter spaces, ADERT overcomes key limitations of traditional sensitivity-based methods and significantly reduces computational cost. Overall, ADERT provides a powerful and extensible platform for next-generation ERT inversion, bridging numerical modelling and modern differentiable programming. Its flexibility makes it well suited for advanced parameterisations, probabilistic inference, and future extensions to multi-physics and three-dimensional problems.

References

Aleardi, M., A. Vinciguerra, and A. Hojat, 2021. A geostatistical markov chain monte carlo inversion algorithm for electrical resistivity tomography. Near Surface Geophysics 19(1), 7–26.

Corrales, M., Berti, S., Denel, B., Williamson, P., Aleardi, M., Ravasi, M., 2025. Annealed stein variational gradient descent for improved uncertainty estimation in fullwaveform inversion. Geophys. J. Int. 241 (2), 1088–1113.

D'Angelo, F., Fortuin, V., 2021. Annealed stein variational gradient descent. In: 3rd Symposium on advances in Approximate Bayesian Inference, pp. 1–12.

Rincón, F., M. Aleardi, A. Tognarelli, and E. Stucchi (2025). Physics-guided deep-learning direct current-resistivity inversion with uncertainty quantification. Geophysics 90(5), E165–E179.

Corresponding author: felipe.rincon@phd.unipi.it

Cross-gradient joint seismic full-waveform and electrical resistivity inversion

F. Rincón[1], M. Aleardi[1], S. Berti[1], A. Tognarelli[1], E. Stucchi[1]
[1] *University of Pisa, Italy*

Introduction

High-resolution imaging of the near-surface is essential for landslide hazard assessment, aquifer characterisation, and geotechnical planning. Geophysical methods offer a non-invasive way to estimate subsurface properties, yet interpretations based on a single parameter are often ambiguous because inverse problems are non-unique and each method has distinct resolution limits. Seismic methods are among the most robust tools for recovering mechanical properties. Near-surface records are typically dominated by high-amplitude surface waves. Conventional method using Multi-channel Analysis of Surface Waves (MASW) extracts dispersion curves to invert for 1-D shear-wave speed (v_s) profiles. While effective for layered media, MASW is challenged by strong lateral heterogeneity and topography. Full Waveform Inversion (FWI) provides a more comprehensive alternative by exploiting the entire seismic wavefield, including scattering and diffraction effects (Fichtner, 2013). Near-surface elastic FWI has demonstrated high-resolution recovery of subsurface models, but it remains sensitive to starting models and strongly nonlinear. Probabilistic and deep-learning approaches have been proposed to mitigate non-uniqueness and quantify uncertainty in inversion problems (Rincón et al. 2025).

Electrical resistivity tomography (ERT) is widely used due to its low cost and sensitivity to porosity, saturation, and fluid pathways (Binley et al., 2015). Standard smoothness-regularised inversions stabilise the ill-posed DC problem but often produce overly smooth anomalies (Loke and Barker, 1996). Recent probabilistic and learning-based strategies improve uncertainty quantification and reduce regularisation bias (Rincón et al., 2025), yet ERT alone remains limited by diffusive sensitivity and a large null-space. Given their complementary sensitivities, joint inversion of seismic and electrical data can reduce ambiguity (Moorkamp, 2017; Rincón et al., 2020; Zhdanov et al., 2021). Most near-surface applications combine Seismic Refraction Tomography (SRT) and ERT (Gallardo and Meju, 2004; Hellman et al., 2017) whereas joint FWI-EM studies remain scarce and are often restricted to synthetic or very shallow settings (Ma et al., 2025). Here we propose a structurally coupled joint inversion of surface-wave FWI and ERT using the cross-gradient operator, avoiding explicit petrophysical assumptions (Wagner et al., 2021). In this paper we present preliminary synthetic results that demonstrate how FWI constraints can sharpen diffusive ERT images and stabilise the recovery of near-surface structure under topography.

Methods

Joint objective function

We consider two model parameter fields: the shear-wave speed model $m_c(i.e., v_s)$ and the resistivity model m_ρ (or equivalently log-resistivity). The joint inversion is formulated as the minimisation of a total objective function:

$$\Phi_{\text{total}}(m_c, m_\rho) = \Phi_{\text{FWI}}(m_c) + \Phi_{\text{ERT}}(m_\rho) + \beta\, \Phi_{\text{XG}}(m_c, m_\rho),$$

where Φ_{FWI} and Φ_{ERT} are least-squares misfit terms (including standard stabilisation/regularisation), Φ_{XG} is the cross-gradient coupling functional, and β is a weighting parameter controlling the strength of structural coupling.

Cross-gradient structural coupling

In 2-D, the cross-gradient is defined as the scalar (out-of-plane) component of the cross product between the spatial gradients of the two parameter fields:

$$t(x,z) = \nabla m_c(x,z) \times \nabla m_\rho(x,z) = \frac{\partial m_c}{\partial x}\frac{\partial m_\rho}{\partial z} - \frac{\partial m_c}{\partial z}\frac{\partial m_\rho}{\partial x}.$$

When $t(x,z) = 0$, the gradients are parallel (or anti-parallel), implying that structural boundaries (changes in v_s and resistivity) align spatially even if the parameter values are not linearly correlated. The coupling term is defined as:

$$\Phi_{\text{XG}}(m_c, m_\rho) = \int_\Omega |t(x,z)|^2 \; d\Omega.$$

This formulation avoids site-specific petrophysical assumptions (e.g., Archie-type relations) while still allowing the two modalities to "communicate" through shared structure.

Forward modelling and gradients

For the seismic component, we model elastic wave propagation and compute gradients using the adjoint-state method (Tarantola, 1984). In practice, this corresponds to correlating the forward wavefield with the back-propagated residual (adjoint) wavefield, yielding $\nabla_{m_c}\Phi_{\text{FWI}}$. Seismic wave propagation and the associated adjoint wavefields are simulated with the spectral-element framework Salvus (Afanasiev et al., 2019), which enables accurate and efficient solution of the elastic wave equation on unstructured meshes. For the ERT component, we solve the Poisson equation and compute sensitivities using the Jacobian–vector machinery available in SimPEG (Cockett et al., 2015), yielding $\nabla_{m_\rho}\Phi_{\text{ERT}}$. The optimisation is performed with L-BFGS-B, which is suitable for large parameter spaces and allows bound constraints.

Complementary resolution illustrated by sensitivity kernels

The rationale for coupling is supported by sensitivity kernels (Fig. 1). Dipole–dipole ERT kernels exhibit broad positive–negative lobes beneath the current and potential dipoles, reflecting the diffusive nature of current flow. Increasing electrode spacing increases depth of investigation but

reduces lateral resolution. Conversely, surface-wave Fréchet kernels at a given frequency are controlled by wavelength: higher frequencies concentrate sensitivity in the shallowest metres, while lower frequencies illuminate deeper regions. At 30 Hz (Fig. 1b), the minimum resolvable wavelength is λ_{min} ~13 m, producing a shallow, high-resolution sensitivity zone. The reference models for both FWI and ERT are taken to be laterally homogeneous and equal to the background value (~ 400 m/s and ~400 $\Omega\,.\,\mathrm{m}$). Therefore, ERT tends to provide stable, depth-reaching but smooth constraints, whereas surface-wave FWI provides higher spatial resolution but stronger nonlinearity and illumination dependence—a natural setting for structural coupling.

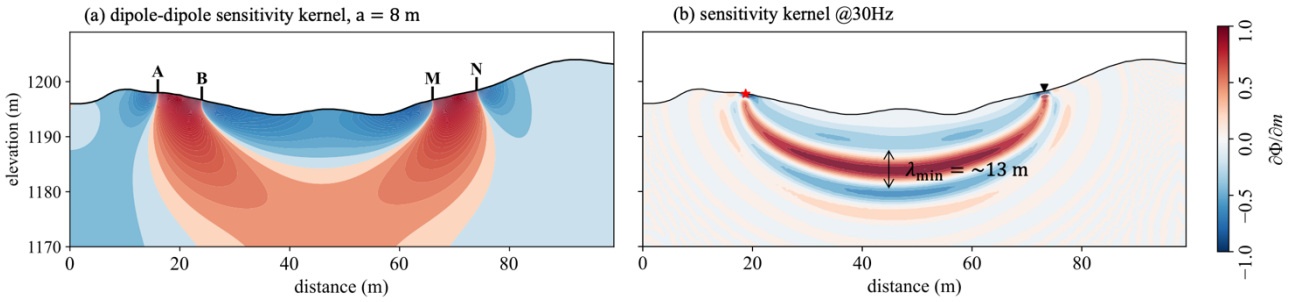

Fig. 1 – Sensitivity kernels illustrating the complementary resolving capacity of electrical and seismic settings: (a) dipole–dipole ERT sensitivity for an electrode spacing of a = 8 m; (b) surface- FWI Fréchet kernel at 30 Hz, highlighting the minimum resolvable wavelength (λ_{min} ~13 m).

Results

We design a synthetic checkerboard experiment where both v_s and resistivity share identical 5×5 m^2 anomalies under realistic topography. Seismic data were simulated with 24 geophones spaced at 4.5 m and 11 vertical-impact sources placed at regular intervals midway between receiver pairs. ERT data were collected on the same line using a dipole–dipole array spaced at 2 m. Starting from laterally homogeneous models, we compute the individual misfit gradients and the cross-gradient field. The FWI gradient (Fig. 2b) shows strong localisation beneath the source–receiver aperture and follows the acquisition illumination: gradient energy concentrates where surface-wave sensitivity is highest, and boundaries of the checkerboard are partially expressed, but weaker illumination regions show reduced recoverability. The ERT gradient (Fig. 2c) is smoother and more diffuse, with broad lobes and limited ability to reproduce small blocks, consistent with DC physics and smoothness regularisation. The cross-gradient term (Fig. 2d) is sharply localised within the anomaly region and suppresses updates outside it, effectively acting as a structural "mask" that promotes coherent changes where both methods expect boundaries. This confirms that Φ_{XG} introduces information that is not contained in either single-physics gradient alone.

We then compare three inversion strategies on synthetic data: FWI-only, ERT-only, and joint FWI–ERT with cross-gradient coupling. The FWI-only inversion (Fig. 3a) recovers several anomalies with relatively sharp boundaries in the best-illuminated zone, but exhibits misplaced or merged blocks and reduced sensitivity at depth, reflecting limited illumination and nonlinearity. The ERT-only inversion (Fig. 3b) captures the broad conductive/resistive trend but strongly smooths the 5×5 m^2 anomalies, leading to low-contrast, laterally smeared features typical of DC inversion with smoothness constraints.

The joint inversion (Fig. 3c–d) yields the most structurally consistent reconstruction: the resistivity model becomes significantly better focused, with sharper block boundaries and reduced smearing

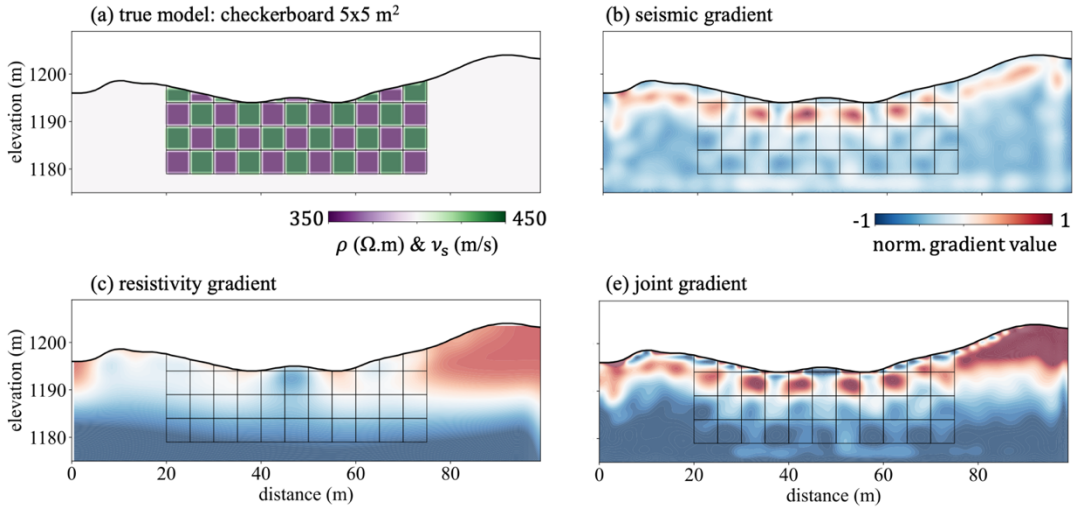

Fig. 2 – Synthetic sensitivity analysis for the checkerboard experiment. (a) True checkerboard model used to generate the seismic and electrical data, consisting of alternating 5 × 5 m^2 anomalies in both v_S and resistivity. (b) Normalised FWI gradient $\nabla m_c \Phi_{FWI}$ computed from a single iteration starting from a homogeneous v_S model. (c) Normalised ERT gradient $\nabla m_\rho \Phi_{ERT}$ obtained from the DC data. (d) Cross-gradient field $\mathbf{t}(x,z)$ highlighting regions where the structural variations in v_S and resistivity are aligned. The comparison illustrates how the cross-gradient term provides strongly localised structural information that is not captured by the individual gradients, thereby motivating its use in the joint inversion framework.

compared with ERT-only, while the recovered v_s model remains comparable in resolution to the FWI-only result. Importantly, anomalies in v_s and resistivity become spatially aligned, indicating that the cross-gradient successfully enforces shared structural trends without imposing a specific functional correlation. Quantitatively (as reported in the synthetic benchmark), the joint approach reduces the resistivity reconstruction error relative to ERT-only while maintaining the seismic reconstruction quality close to the standalone FWI case, demonstrating that the framework effectively exploits complementary sensitivities.

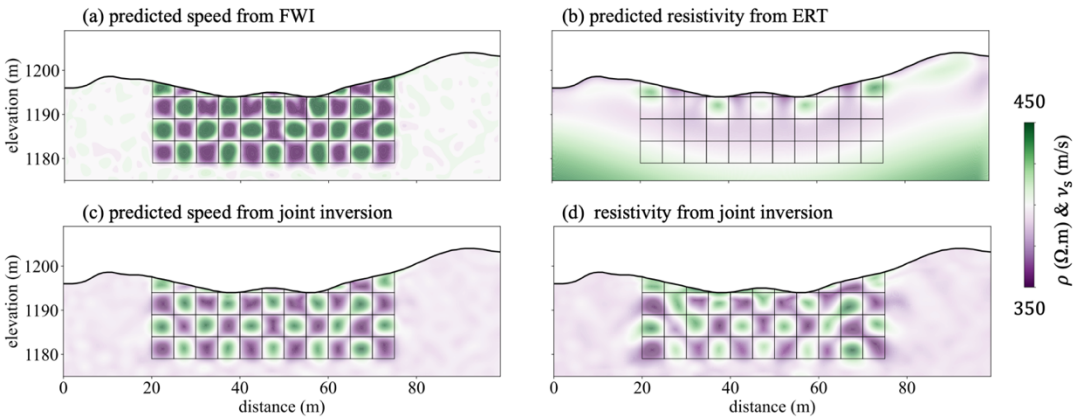

Fig. 3 – Synthetic inversion results for the checkerboard experiment. (a) FWI-only inversion of the shear-wave speed v_s. Several anomaly blocks are partially recovered, but the solution exhibits merged or misplaced structures and reduced sensitivity at depth, with a relative error of 0.41% with respect to the true model. (b) ERT-only inversion of the resistivity field. The diffusive nature of DC data and smoothness regularisation smear out the 5×5 m 2 anomalies, yielding a broad low-contrast region and a relative error of 0.81%. (c) Joint FWI–ERT inversion result for V S obtained

using the cross-gradient constraint. The anomaly blocks are more sharply resolved and better aligned with the true geometry. (d) Corresponding joint resistivity model, where the anomalies are significantly better focused and structurally consistent with the recovered v_s field. The joint inversion achieves the lowest errors, with relative misfits of 0.44% for V S and 0.49% for resistivity, demonstrating the benefits of exploiting the complementary sensitivities of the two methods.

Conclusion

These preliminary synthetic results show that cross-gradient coupling provides an effective, petrophysics-free mechanism for joint surface-wave FWI–ERT imaging. Sensitivity kernels highlight the complementary resolving capacity of the two methods: FWI supplies high-resolution, wavelength-controlled structural information, while ERT contributes stable depth sensitivity but suffers from smoothing bias. The checkerboard experiments demonstrate that the cross-gradient term adds focused structural guidance that improves resistivity recovery and promotes consistent multiphysics interpretation. Ongoing work extends the method to field data from an active landslide complex.

References

Afanasiev, M., Boehm, C., van Driel, M., Krischer, L., Rietmann, M., May, D.A., Knepley, M.G. and Fichtner, A. (2019) Modelling the propagation of seismic waves using SEMLib: a spectral-element method library for large-scale seismic wave propagation. Geophysical Journal International, 216(3), pp. 1675–1692. doi: 10.1093/gji/ggy469.

Binley, A., Hubbard, S.S., Huisman, J.A., Revil, A., Robinson, D.A., Singha, K. and Slater, L.D. (2015) The emergence of hydrogeophysics for improved understanding of subsurface processes. Water Resources Research, 51(6), pp. 3837–3866. doi: 10.1002/2015WR017016.

Cockett, R., Kang, S., Heagy, L.J., Pidlisecky, A. and Oldenburg, D.W. (2015) SimPEG: An open source framework for simulation and gradient based parameter estimation in geophysical applications. Computers & Geosciences, 85, pp. 142–154.

Fichtner, A. (2013) Full Seismic Waveform Modelling and Inversion. Berlin: Springer. doi: 10.1007/978-3-642-13846-3.

Gallardo, L.A. and Meju, M.A. (2004) Joint two-dimensional DC resistivity and seismic travel time inversion with cross-gradients constraints. Journal of Geophysical Research, 109(B3), B03311. doi: 10.1029/2003JB002716.

Hellman, K., Ronczka, M., Günther, T., Wennemann, F. and Rücker, C. (2017) Structural joint inversion of ERT and refraction seismic data in an alpine permafrost environment. Journal of Applied Geophysics, 146, pp. 26–37.

Loke, M.H. and Barker, R.D. (1996) Rapid least-squares inversion of apparent resistivity pseudosections using a quasi-Newton method. Geophysical Prospecting, 44(1), pp. 131–152. doi: 10.1111/j.1365-2478.1996.tb00142.x.

Ma, J., Deng, Y., Li, X., Guo, R., Zhou, H. and Li, M. (2025) Recent advances in machine learning-enhanced joint inversion of seismic and electromagnetic data. Surveys in Geophysics, 46, pp. 197–225. doi: 10.1007/s10712-024-09867-3.

Moorkamp, M. (2017) Integrating electromagnetic data with other geophysical observations for enhanced imaging of the Earth: A tutorial and review. Surveys in Geophysics, 38(5), pp. 935–962. doi: 10.1007/s10712-017-9413-7.

Rincón, F., Monsalve, G. and Uhlemann, S. (2020) DC resistivity and seismic refraction define surface ruptures in tropical soils—A case study of La Bonita, Antioquia, Colombia. In: AGU Fall Meeting Abstracts (2020), NS004–04.

Rincón, F., Berti, S., Aleardi, M., Tognarelli, A. and Stucchi, E., 2025. Integrating deep learning and discrete cosine transform for surface waves full-waveform inversion. Geophysical Journal International, 240(1), pp.805-828.

Rincón, F., Aleardi, M., Tognarelli, A. and Stucchi, E. (2025) Physics-guided deep learning DC-resistivity inversion with uncertainty quantification. Geophysics, 90(5), pp. E165–E179.

Tarantola, A. (1984) Inversion of seismic reflection data in the acoustic approximation. Geophysics, 49(8), pp. 1259–1266.

Wagner, F.M. and Uhlemann, S. (2021) An overview of multimethod imaging approaches in environmental geophysics. In: Advances in Geophysics, 62, pp. 1–72. doi: 10.1016/bs.agph.2021.06.001.

Zhdanov, M.S., Jorgensen, M. and Cox, L. (2021) Advanced methods of joint inversion of multiphysics data for mineral exploration. Geosciences, 11(6), 262. doi: 10.3390/geosciences11060262.

Corresponding author: felipe.rincon@phd.unipi.it

Airborne Gravity Field Mapping over Italy with Strapdown Gravimetry: Methodology and Preliminary Results

D. Sampietro[1,2], A. Santoni[1], M. Capponi[1], M. Arciero[3], L. Lingesso[4], L. Rampa[5], F. Bocchino[6], A. M. De Pace[6], S. Pecora[7]

[1] Geomatics Research & Development s.r.l., Lomazzo (CO), Italy;

[2] Istituto Nazionale di Geofisica e Vulcanologia, Catania (CT), Italy;

[3] eGeos S.p.A, Roma (RM), Italy;

[4] CGR SpA, Parma (PR), Italy;

[5] I-R-S Italian Remote Sensing s.r.l., Montefalcone nel Sannio (CB), Italy;

[6] DICEA, Sapienza Università di Roma, Roma (RM), Italy;

[7] Ministero dell'Ambiente e della Sicurezza Energetica, Roma (RM), Italy;

Recent advances in inertial sensors have enabled the operational use of strapdown systems for airborne gravity-field acquisition achieving accuracy levels and spatial resolution suitable for geodetic and geophysical applications. Instruments such as the iMAR iCORUS-2 gravimeter integrate high-performance accelerometric sensors, thermal control systems, and GNSS receivers, allowing continuous acquisition of gravimetric data during flight without traditional stabilized mechanisms. These capabilities enable dense, methodical airborne gravity surveys that can rapidly span extensive regions while maintaining mGal-level accuracy (1 mGal = 10^{-5} m/s²). The resulting gravity data are well suited for subsurface modelling and for determining geodetic reference surfaces such as the geoid.

Within this framework, the *Ministero dell'Ambiente e della Sicurezza Energetica* (MASE), under the National Recovery and Resilience Plan, is implementing a national program for the integrated production of a digital terrain model and a gravity-field model covering the entire Italian territory. The initiative pursues two main goals: the generation of a new Digital Surface Model and Digital Terrain Model (DSM, DTM) based on high-resolution LiDAR data (10 points/m²), and the development of a new, homogeneous, high-resolution airborne gravity dataset together with the associated geoid model. These outputs constitute an essential element of the National Integrated Surveillance and Monitoring System (SIM — Sistema Integrato di Monitoraggio).

Focusing on the airborne gravity surveys, data acquired by the inertial system—specifically accelerations and angular rates sampled at 400 Hz—were integrated with magnetometer readings (also at 400 Hz) and GNSS data (sampled at 5 Hz) using a direct estimation method (Johann et al., 2019). In details, once the aircraft trajectory and attitude are determined via a Kalman filter, the inertial accelerations are aligned to the vertical component and then combined with accelerations derived from GNSS to obtain an initial gravity estimate. This preliminary gravity signal is finally processed with the filtering strategy proposed by Sampietro et al. (2017).

Two test regions, covering the northern Tuscan–Emilian Apennines and the Maremma Laziale areas, have been acquired and processed. Results show the possibility to derive gravity-field grids achieving accuracies of about 1 mGal and a spatial resolution better than 2.5 km.

Acknowledgements

Thanks are extended to *Ministero dell'Ambiente e della Sicurezza Energetica* for granting authorization to present results related to the test areas. The authors also acknowledge Prof. Mattia Crespi and Dr. Paolo Benelli for the valuable discussions during the results verification phase.

References

Johann, F., Becker, D., Becker, M., Forsberg, R., & Kadir, M. (2019). The direct method in strapdown airborne gravimetry–a review. ZfV-Zeitschrift für Geodäsie, Geoinformation und Landmanagement, (zfv 5/2019).

Sampietro, D., Capponi, M., Mansi, A. H., Gatti, A., Marchetti, P., & Sansò, F. (2017). Space-Wise approach for airborne gravity data modelling. Journal of geodesy, 91(5), 535-545.

Corresponding author:

Daniele Sampietro

daniele.sampietro@g-red.eu

Seismic interferometry in surface-borehole systems: effects of sensor geometry and downgoing wavefields

A. Schibuola[1], S. Parolai[1], R. Amiri Fard[1], M. Possenelli[2], R. Morga[2], F. Baldassi[1], F. Romanelli[1], S.-T. Lai[3]

[1] *Università degli Studi di Trieste (Department of Mathematics, Informatics and Geosciences, Italy)*
[2] *Università degli Studi di Bari (Department of Earth and Geo-environmental Sciences, Italy)*
[3] Université Gustave Eiffel (Cité Descartes, 77447 Marne-la-Vallée Cedex 2, France)

Local site conditions can markedly influence earthquake ground motion by controlling amplification, duration, and spatial variability. When shaking is sufficiently strong, near-surface soils may enter a nonlinear regime in which large strains modify their mechanical properties, decreasing shear modulus and increasing damping, and may even trigger liquefaction or permanent deformation.

In situ nonlinear site response can be inferred from surface-borehole seismic recordings through observed frequency changes, such as empirical transfer functions, or velocity changes estimated via seismic interferometry. However, the magnitude of these variations may be influenced by factors beyond the intrinsic nonlinear behavior of near-surface materials.

Since nonlinear effects are typically concentrated in shallow layers, it remains unclear how the response of the entire soil column between surface and borehole sensors contributes to the observed measurements. In particular, the dependence of inferred velocity changes on the separation between surface and borehole instruments is not well constrained. Additionally, the contribution of the downgoing wavefield at borehole sensors may further affect the interpretation of interferometric results.

To address these questions, we develop a one-dimensional numerical modeling framework to investigate how seismic interferometry captures velocity variations under different site response regimes. Both equivalent-linear and fully nonlinear constitutive behaviors are considered to explore their impact on interferometric observables.

By systematically varying the distance between surface and borehole sensors and the depth distribution of velocity changes, we aim to clarify the sensitivity, limitations, and interpretability of interferometry-based velocity monitoring for nonlinear site response studies. This ongoing work

provides methodological guidance for the analysis and design of surface–borehole seismic deployments.

Corresponding author: ALESSANDRA.SCHIBUOLA@units.it

Investigating Borehole TDIP Response in the Ivrea-Verbano Zone (ICDP-DIVE project): Linking Chargeability to Mineral Distribution from SEM and MicroCT Data

Ventola I.[1], Caspari E. [2], Greenwood A. [2], Hawemann F. [1], Venier M. [1], Toy V. [1]

[1] Johannes Gutenberg Universität Mainz, Mainz, Germany
[2] Montanuniversität Leoben, Leoben, Austria

As part of a multidisciplinary effort to characterize the deep continental crust, two scientific boreholes were drilled in the Ivrea Verbano Zone (IVZ, Western Alps, Italy), one of the few near-complete continental crustal sections exposed on Earth's surface (Pistone et al. 2020). The boreholes were realized within the Drilling the Ivrea Verbano ZonE (DIVE) project, supported by the International Continental Scientific Drilling Program (ICDP-5071; Li et al. 2024). Among various in-situ measurements, time-domain induced polarization (TDIP) surveys were conducted in both wells, acquiring borehole chargeability data with two electrode spacings (16" and 64").

The boreholes intersect a wide range of lithologies hosting sulfides and oxides, either disseminated or concentrated along veins and fractures, which represent potential sources of chargeable response. A set of 11 samples from these boreholes was previously analyzed for petrological and structural purposes using both scanning electron microscopy (SEM) and micro-computed tomography (microCT). Starting from these analyses, the study seeks to understand and, where feasible, quantify the role of specific petrophysical properties in shaping borehole chargeability.

The following petrophysical characteristics have been evaluated so far: the abundance of metallic minerals (expressed as volume and area fractions), the perimeter-to-area and surface-to-volume ratios, the connectivity density, and the preferred orientation of these conductive phases.

Preliminary observations suggest that:

- Borehole chargeability is not simply proportional to the abundance of metallic minerals;
- As intuitively expected from polarization theory, the number of active surfaces plays a dominant role over the total volume;
- The preferred orientation of conductive phases appears to be a key factor influencing the measured chargeability;
- The presence of other mineral phases, such as graphite, may mask or amplify the response of metallic minerals depending on their structural relationship.

While no deterministic relationship has been identified at this stage, this work outlines a potential path to improve the interpretation of TDIP data in mineralized systems and to define complementary yet efficient tools for assessing the economic potential of deep rock formations in the context of mineral exploration.

References

Li, J., E. Caspari, A. Greenwood, et al. 2024. “Integrated Rock Mass Characterization of the Lower Continental Crust Along the ICDP-DIVE 5071_1_B Borehole in the Ivrea-Verbano Zone.” *Geochemistry, Geophysics, Geosystems* 25 (12): e2024GC011707. https://doi.org/10.1029/2024GC011707.

Pistone, Mattia, Luca Ziberna, György Hetényi, Matteo Scarponi, Alberto Zanetti, and Othmar Müntener. 2020. “Joint Geophysical-Petrological Modeling on the Ivrea Geophysical Body Beneath Valsesia, Italy: Constraints on the Continental Lower Crust.” *Geochemistry, Geophysics, Geosystems* 21 (12): e2020GC009397. https://doi.org/10.1029/2020GC009397.

Bayesian inversion of 3D Electrical Resistivity Tomography data using a subspace reparameterization approach

Alessandro Vinciguerra[1], Guy Marquis [1]

[1] *Université de Strasbourg, CNRS, Institute Terre ed Environnement de Strasbourg, France*

1 Introduction

Electrical Resistivity tomography (ERT) is a geophysical method widely used in near-surface and mining exploration. The associated inverse problem is ill-conditioned, with the number of unknowns exceeding the number of data points, and is nonlinear, which leads to non-uniqueness of the solution. These issues become more severe in the case of 3D inversion, where the number of uknowns increases dramatically due to the three-dimensional discretization of the half-space. For these reasons can be relevant to evaluate the reliability of the solution through the estimation of the associated uncertainty. In order to estimate the uncertainty, an efficient ensemble-based algorithm which is feasible for 3D inversion. The Ensemble-based algorithms, and in particular the Ensemble Smoother Multiple Data Assimilation by Emerick and Reynolds 2013, has been succesfully applied by Vinciguerra et al., 2024 and Vinciguerra et al., 2025 in near surface and mining exploration ERT data inversion to approximate the posterior probability density function (*pdf*) associated with the 2D inverse problem solution. Usually, in case of 3D inversion, the number of parameters increases exponentially with the dimension of the model, giving rise to time consuming inversion, and increment of the required memory (Loke et al., 2022). Consequently, Bayesian inversion is rarely used for full 3D problems due to the huge computational burden needed. To address these issues, reparameterization strategies can be employed, such as the Discrete Cosine transform and the Wavelet transform (Loke et al., 2022), which reduces the number of model parameters and, consequently, the computational cost and required memory. However, because those transformations are lossy, they lead to a loss of spatial resolution, particularly when the model space is significantly reduced. For this reason, in this work we propose an alternative strategy to reduce the model space and make the Bayesian inversion feasible for the 3D inversion. Specifically, we employ a subspace ensemble-based algorithm developed by Raanes *et al., 2019* and Evensen *et al.*, 2019 which has already been applied to reservoir history matching and oceanography. This approach recasts the problem by seeking the solution within the subspace spanned by the prior ensemble of models. As a test about feasibility of the Bayesian approach we apply the algorithm to synthetic 3D model composed by two targets of different resistivity within an homogeneous half-space.

2 Methods

The target *pdf* could be approximated through an ensemble-based method minimising an ensemble of cost functions for each realization as:

$$T(m_j) = \frac{1}{2}\left(m_j - m_j^p\right)^T C_m^{-1}\left(m_j - m_j^p\right) + \frac{1}{2}\left(g(m_j) - d_j\right)^T C_d^{-1}\left(g(m_j) - d_j\right) \quad (1)$$

where m_j is the j-th ensemble member, m_j^p is the j-th ensemble member of the prior ensemble, g is the forward operator, C_m is the model covariance matrix, C_d is the data covariance matrix of dimension mxm and d_j is the observed data of dimension m. Since our objective is to search for the solution within the ensemble subspace (Evensen et al., 2019, Raanes et al., 2019), we define the prior ensemble of model as:

$$M = \left(m_1^p, m_2^p, \ldots, m_N^p\right) \quad (2)$$

with N_E size of the ensemble and we define the zero-mean anomaly matrix as:

$$A = M\left(I_{N_E} - \frac{1}{N_E}11^T\right)/\sqrt{(N_E - 1)} \quad (3)$$

where $1 \in \mathbb{R}^N$ is a vector of ones, I_{N_E} is the identity matrix of dimension $N_E x N_E$, the matrix $I_{Ne} - \frac{1}{N_e}$ subtract the mean from M. Evensen et al., 2019 and Raanes et al., 2019 suggests that the solution is confined to the space spanned by the prior ensemble. Thus, we will search for the solution in that space assuming that an updated ensemble M^u is equal to the prior ensemble, M^p plus a linear combination of ensemble anomalies A,

$$M^u = M^p + AW \quad (4)$$

where W has dimension $N_E x N_E$, then we rewrite the cost function for the j-th column of W as

$$T(w_j) = \frac{1}{2}w_j^T w + \frac{1}{2}\left(g(m_j) - d_j\right)^T C_d^{-1}\left(g(m_j) - d_j\right) \quad (5)$$

Evensen et al., 2019 suggests that minimizing (5) corresponds find the minima of the original cost function (1) but restricted on the ensemble subspace. Thus, we are now searching for a solution in a much smaller model space, solving for the N_E vectors $w_j \in \mathbb{R}^{N_E}$.

2.1 Sensitivity approximation

To minimize the cost function in (5), our strategy is to employ a Gauss-Newton method for each ensemble member, approximating the jacobian from the ensemble of models and data. In particular, we compute the average sensitivity S at iteration i from the ensembles by linear regression as (Evensen et al., 2019):

$$S_i = Y_i \Omega_i^{-1} \quad (6)$$

where

$$Y_i = g(X_i)\left(I_{N_E} - \frac{1}{N_E}11^T\right)/\sqrt{(N_E - 1)} \quad (7)$$

is the predicted data ensemble anomalies, whereas Ω_i is:

$$\Omega_i = I + W_i\left(I_{N_E} - \frac{1}{N_E}11^T\right)/\sqrt{(N_E - 1)} \quad (8)$$

Thus, we can write the ensemble of models update at iteration i as:

$$W_{i+1} = W_i - \gamma(W_i - S_i^T(S_i S_i^T + C_d)^{-1}H) \qquad (9)$$

where $\gamma \in (0,1]$ is the step length parameter and H is

$$H = S_i W_i + D - g(M_i) \qquad (10)$$

where D the ensemble of perturbed observed data. In terms of dimensionality, the matrix W_i has dimension $N_E x N_E$, the average sensitivity has dimension mxN_E and H has dimension mxN_E. From the equations above it is evident that the reformulation of ensemble based in the subspace domain is able to reduce the model space dimension, linking the size of the ensemble to the number of unknowns of the problem.

Synthetic test

To test the approach we build a simple model composed by two spheres of radius 165 m at depth of 100 m and having a resistivity of 10 $\Omega \cdot m$ and 1000 $\Omega \cdot m$ embedded in a homogeneous half-space of 100 $\Omega \cdot m$ (Cockett et al., 2015). The model is discretized using an octree mesh, in which cell dimensions are powers of two larger than a prescribed base cell size, thereby keeping the total number of cells computationally feasible (Cockett et al., 2015). The modelling domain has dimension x, y, z of 8000, 8000, 4000 m for a total number of 85026 tetraedrical cells, whereas the inversion mesh is composed by 71176 cells. The data is simulated through Simpeg open source library (Cockett et al) with a dipole-dipole configuration composed by six lines, which performs a 3D acquisition. We generate the prior ensemble of models using GSTools library (Müller et al., 2022), adopting a Gaussian random field generator in accordance with the assumption of prior Gaussianity. As described in the previous section (Equation 5 and 9), the ensemble size directly determines the number of unknowns of the inverse problem. Consequently, its choice has to be a compromise between computational cost, model space dimension and robust approximation of the *pdf.* In this example, we generate an ensemble of 2000 models, which substantially reduces the model space from 71176 to 2000. The inversion algorithms converges in few iterations for a total computational time of 13 hours in a laptop equipped with Intel Core i7-1165G7 @ 2.80GHz. Both targets are well recovered, as indicated by model slices normal to the Y-axis (Fig. 1c) and to the Z-axis (Fig. 1d). Moreover, the root mean square error of the predicted data is 3.3%. The ensemble-based inversion provides an approximation of the *pdf,* from which we can represent the standard deviation as a 3D volume (Fig. 2a, clip normal to the Y axis) or as marginal distributions associated with individual model cells. Fig. 2b illustrates the marginal distribution corresponding to a tetrahedral cell of the homegeneous half-space, whereas Fig. 2c, 2d and Fig. 2e and 2f display one of the marginals *pdf* of the high-resistivity and low-resistivity sphere, respectively. Fig. 2a, which represents the standard deviation volume corresponding to the clip of Fig. 1c, exhibits low values of standard deviation close to the surface.

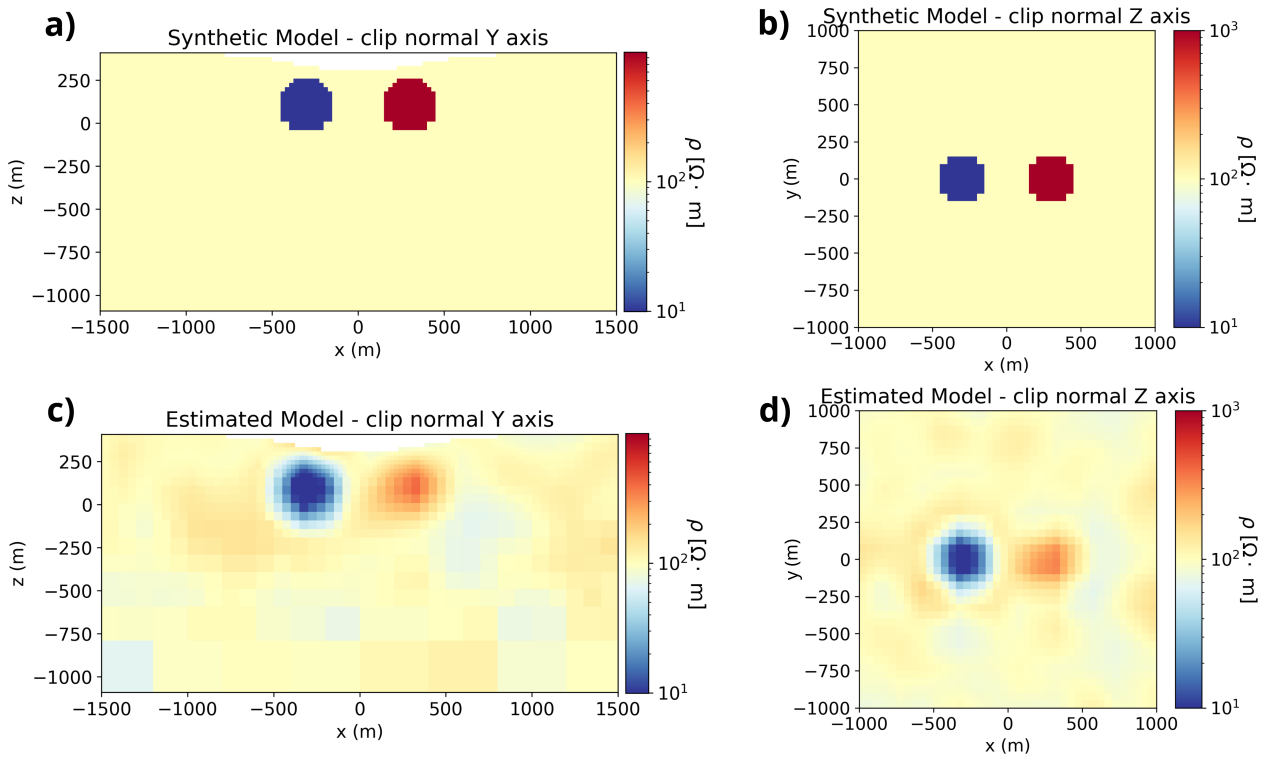

Fig. 1 – a) Clip of the 3D synthetic model perpendicular to Y axis. b) Clip of the 3D synthetic model perpendicular to Z axis. c) Estimated mean model, clip normal to the Y axis. d)Estimated mean model, clip normal to the Z axis.

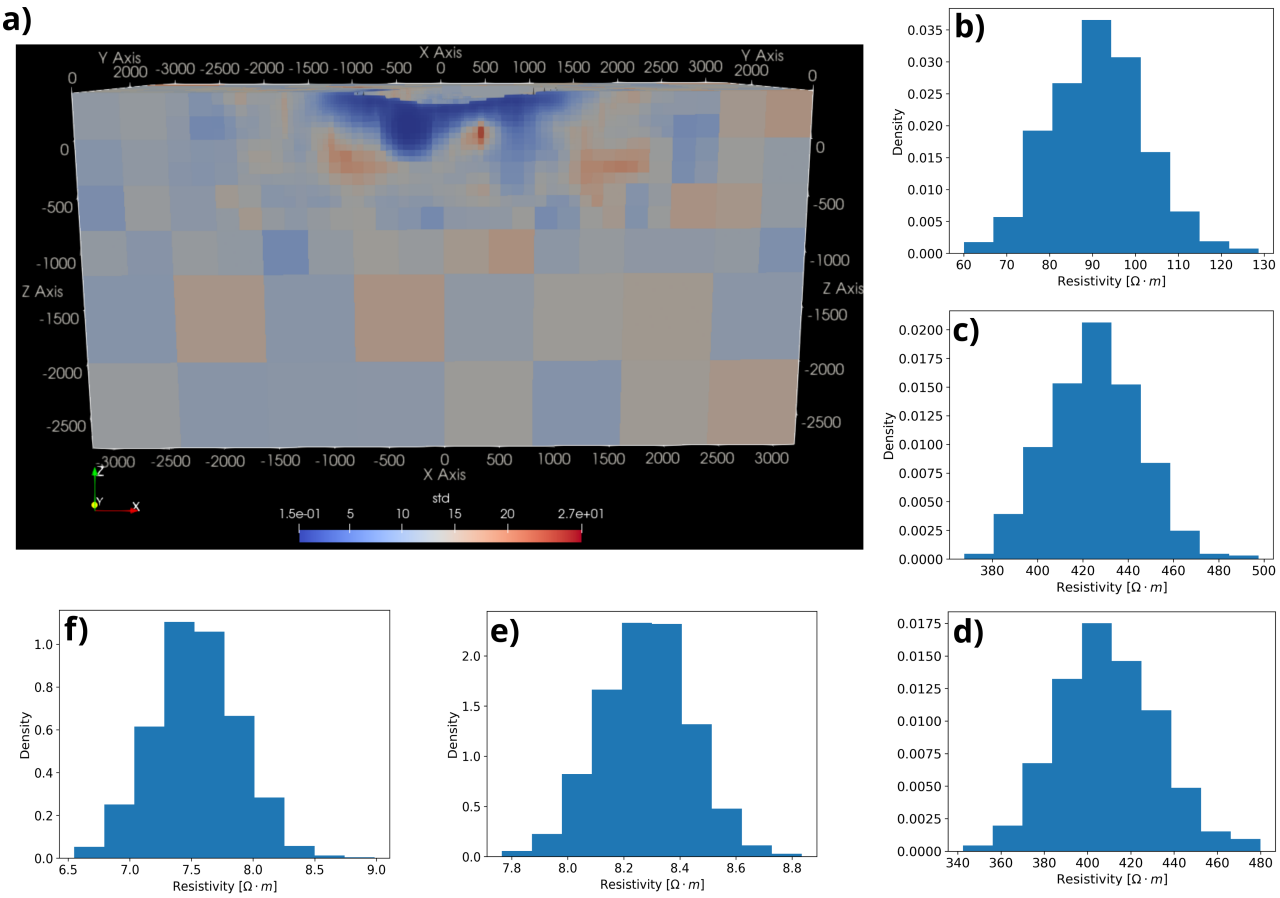

Fig. 2 – a) Volume of standard deviation values b) Marginal *pdf associated with* the homogeneous half-space c) and d) Marginal *pdfs associated with the high resistive sphere. e) and f) Marginal pdfs associated with the low resistive sphere.*

Conclusions

This work introduces an alternative approach to invert ERT data in the Bayesian framework in a large model space dimension without using lossy transform methods. As suggested by the 3D synthetic test, where the anomaly shapes are reasonably well reconstructed in a feasible computational time, the subspace ensemble-based algorithm appears promising for mitigating ill-conditioning of the problem and reducing the computational cost. Moreover, uncertainty quantification, expressed as a volume of standard deviations or 3D posterior realizations, can be used to identify the most reliable regions of the model.

References

Cockett, R., Kang, S., Heagy, L.J., Pidlisecky, A., and Oldenburg, D.W. 2015. SimPEG: An open source framework for simulation and gradient based parameter estimation in geophysical applications. Computers and Geosciences. Vol. 85. https://doi.org/10.1016/j.cageo.2015.09.015

Emerick A.A., and Reynolds, A.C. 2013. Ensemble Smoother with multiple data assimilation. Computers and Geosciences. Vol. 55. https://doi.org/10.1016/j.cageo.2012.03.011

Evensen, G., Raanes, P.N., Stordal, A.S, and Hove, J; 2019. Efficient Implementation of an Iterative Ensemble Smoother for Data Assimilation and Reservoir History Matching. Frontiers in Applied Mathematics and Statistics. Vol. 5. https://doi.org//10.3389/fams.2019.00047.

Loke, M.H. and Wilkinson, P.B. and Kuras, O. and Meldrum, P.I. and Rucker, D.F. 2022. The use of a semi-structured finite-element mesh in 3-D resistivity inversion. Geophysical Prospecting. Vol.70. https://dx.doi.org/10.1111/1365-2478.13260

Müller, S., Schüler, L., Zech, A., and Heße, F; 2022: GSTools v1.3: a toolbox for geostatistical modelling in Python, Geosci. Model Dev., 15, 3161–3182, https://doi.org/10.5194/gmd-15-3161-2022, 2022.

Raanes, P.N., Stordal, A.S., and Evensen, A; 2019. Revising the stochastic iterative ensemble smoother. Copernicus GmbH. https://doi.org//10.5194/npg-2019-10

Vinciguerra, A., Aleardi, M., Madsen, L.M., Bording, T.S., Christiansen, A.V. and Stucchi, E. 2024. Stochastic inversion of time-lapse electrical resistivity tomography data by means of an adaptive ensemble-based approach. Geophysical Prospecting. Vol.72. https://doi.org/10.1111/1365-2478.13464

Vinciguerra, A., Marquis, G., and Girard, J. 2025. Localized Ensemble-Based Inversion of ERT Data: Synthetic Test and Application to Mining Exploration. EAGE Annual Meeting. https://doi.org/10.3997/2214-4609.202510913.

Corresponding author: avinciguerra@unistra.fr

A theoretical lower bound for the saturation exponent in Archie's law

H Yan[1], C Comina[1], S C Vinciguerra[1]

[1] *Department of Earth Science, University of Turin, Turin, Italy*

Introduction

Archie's law is one of the most widely employed methods for the determination of electrical conductivity of partially saturated porous media. The traditional Archie's law (Archie, 1942) and the modified one (Glover et al., 2000) hold the following forms:

$$\sigma_{unsat} = \sigma_w \phi^m S_w^n, \quad (1)$$

$$\sigma_{unsat} = \sigma_w \phi^m S_w^n + \sigma_s \left(1 - \phi^m\right), \quad (2)$$

where σ_{unsat} is the conductivity of the overall unsaturated porous medium; σ_w and σs are the conductivities of the pore water and the solid grains respectively; ϕ is the porosity; S_w is the water saturation; m is the cementation exponent and n is the saturation exponent. Archie law is highly dependent on the appropriate selection of *m* and more importantly of *n*. Several experimental results illustrate that *n* is approximately 2 for the majority of water saturated rocks (e.g., Mavko et al., 2009). Although *n* has been considered constant and unrelated to saturation levels, some new perspectives suggest that *n* should vary with saturation (e.g., Worthington & Pallatt, 1992; Glover, 2017). We analyzed a database of some representative resistivity measurements performed on partially saturated water-wetted porous media (Weerts et al., 1999; Han et al., 2009; Tang 2019; Han et al., 2020; Mustofa et al., 2022; Pang et al., 2024) and evaluated the variability of *n* for different saturation levels. The obtained results show that *n* under a given degree of saturation can be less than 1.5 and even less than 1. Such "abnormal" saturation exponent value indicates that new constraints on the saturation exponent value are required. This work aims to define such constraints, by proposing a theoretical lower bound for the saturation exponent (denoted as LBSE here).

Theory

We assume that the pore water adheres to the solid surface and it is fully and homogeneously connected. The solid matrix is idealized as a series of spheroidal grains with a specific aspect ratio, and residual water is considered as a uniform film adhering to the grain surfaces. The effect of the water on the solid grains is represented as a modification in their shapes. These shape-modified spheroids are subsequently employed to calculate the cementation exponent of the pore space occupied by air (or oil). The water saturation exponent is then determined by quantifying the connectedness of the residual water adhering to the solid surface. The obtained saturation exponents vary with saturation and are here considered as a theoretical lower bound,

corresponding to the highest water connectivity. The microstructure of our hypothesized unsaturated porous medium is shown in Figure 1a. A similar structure has been reported in Fukue et al., (1999). The water film is assumed adhering homogeneously at the grains' surface (Figure 1b).

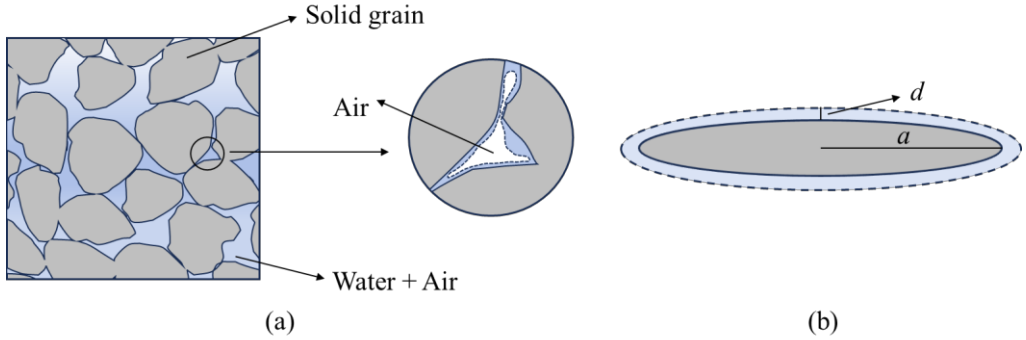

Fig. 1 – (a) A schematic representation of the water distribution in the pore space according to our assumptions; (b) A schematic representation of the water film surrounding the spheroidal grain.

Following derivation, we propose a formulation of the LBSE in the form:

$$LBSE = \frac{\ln\left[\phi^m - \left(\phi - \phi S_w\right)^i\right]}{\ln\left(\phi S_w\right)}\left(\frac{\ln\phi}{\ln S_w}+1\right) - m\frac{\ln\phi}{\ln S_w}, \quad (3)$$

where ϕ is the porosity; m is the cementation exponent; S_w is the saturation. The parameter i is the cementation exponent of the residual pore space, which can be expressed by the aspect ratio β of deformed grains:

$$i = \frac{5 - 3\left[\frac{1}{1-\beta^2} - \frac{\beta}{\left(1-\beta^2\right)^{3/2}}\arccos\beta\right]}{3 - 3\left[\frac{1}{1-\beta^2} - \frac{\beta}{\left(1-\beta^2\right)^{3/2}}\arccos\beta\right]^2}. \quad (4)$$

The aspect ratio β can be obtained by solving the following cubic equation:

$$\left(\frac{\beta-\alpha}{1-\beta}\right)^3 + (\alpha+2)\left(\frac{\beta-\alpha}{1-\beta}\right)^2 + (2\alpha+1)\left(\frac{\beta-\alpha}{1-\beta}\right) - \frac{\phi\alpha S_w}{(1-\phi)} = 0. \quad (5)$$

This step can be easily simplifies by built-in functions in some general mathematical software.

In equation 5, α is the original aspect ratio of the grains, which can be calcualted by solving the following equation:

$$\frac{3+\sqrt{36m^2-60m+9}}{6m} = \frac{1}{1-\alpha^2} - \frac{\alpha}{\left(1-\alpha^2\right)^{3/2}}\arccos\alpha. \quad (6)$$

Although there is no closed-form expressions for α, it can be calculated from m by some inversing programs.

According to the lower bound of the saturation exponent (eq. 3), the lower bound of resistivity (denoted as *LBR*) can be determined as follows:

$$LBR = \left[\frac{\phi^m S_w^{LBSE}}{R_w} + \frac{1-\phi^m}{R_s} \right]^{-1} . \quad (7)$$

Validation

The saturation exponent from literature data is used to verify our proposed lower bound. Since the calculated lower bound of n is related to the cementation exponent m, the bound varies among different samples. To plot all the data points in a single figure, we analyse the difference between the real saturation exponents and the theoretical lower bounds:

$$e = n_{real} - LBSE . \quad (8)$$

The proposed lower bound can be validated if e is always positive for all data points. As shown in Figure 2a, nearly all data points lie above zero, with only a data falling below 0, likely due to experimental uncertainty. This distribution supports the validity of the proposed lower bound.

Figure 2b compares the resistivity lower bound from our LBSE against the HS bound. All data lie above our bound except one close to it, in agreement to Figure 3a. In contrast, the HS bound is below the data only at low saturation, while it reverses the position with respect the data at high saturation. This shows that the LBSE proposed in this work provides a more reliable reference for the electrical properties of unsaturated porous media, further confirming its accuracy and applicability.

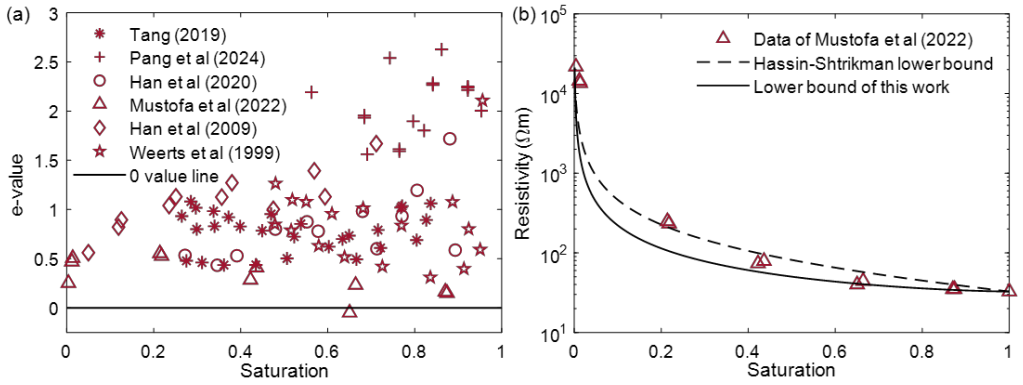

Fig. 2 –(a) The calculated differences between the real saturation exponents of the datasets and their correspondent lower bounds; (b) Comparison between our lower bound of resistivity and the HS lower bound. The data points are from Mustofa et al., (2022).

Conclusion

In this work, a theoretical lower bound of the saturation exponent in Archie's law for partially saturated porous media has been developed. The bound depends on saturation, porosity, and

cementation exponent, and it was validated against existing data and the HS bound. It was theoretically shown that the saturation exponent in water-wetted media can be less than 1, indicating its range should not be limited to more than 1. Although the proposed LBSE does not provide exact values, it offers a useful reference for experiments. Testing values below this bound may induce errors in other parameters such as porosity or phases' resistivities.

Acknowledgments

This work was financially supported by the China Scholarship Council, No.202308620146.

References

Archie, G. E. (1942). The electrical resistivity log as an aid in determining some reservoir characteristics. *Transactions of the AIME, 146*(1), 54–62. https://doi.org/10.2118/942054-G

Fukue, M., Minato, T., Horibe, H., & Taya, N. (1999). The micro-structures of clay given by resistivity measurements. *Engineering Geology, 54*, 43–53. https://doi.org/10.1016/S0013-7952(99)00060-5

Glover, P. W. J., Hole, M. J., & Pous, J. (2000). *A modified Archie's law for two conducting phases*. *Earth and Planetary Science Letters, 180*(3–4), 369–383. https://doi.org/10.1016/S0012-821X(00)00168-0

Glover, P. W. J. (2017). A new theoretical interpretation of Archie's saturation exponent. *Solid Earth, 8*, 805–817. https://doi.org/10.5194/se-8-805-2017

Han, T., Liu, S., Xu, D., & Fu, L.-Y. (2020). Pressure-dependent cross-property relationships between elastic and electrical properties of partially saturated porous sandstones. *Geophysics, 85*(3), MR107–MR115. https://doi.org/10.1190/geo2019-0477.1

Mavko, G., Mukerji, T., & Dvorkin, J. (2009). *The Rock Physics Handbook: Tools for Seismic Analysis of Porous Media* (2nd ed.). Cambridge University Press. https://doi.org/10.1017/CBO9780511626753

Mustofa, M. B., Fauzi, U., Latief, F. D. E., & Warsa, W. (2022). Experimental and modeling of electrical resistivity changes due to micro-spatial distribution of fluid for unconsolidated sand. *Journal of Petroleum Science and Engineering, 208*, 109472. https://doi.org/10.1016/j.petrol.2021.109472

Pang, M., Ba, J., Carcione, J. M., & Saenger, E. H. (2024). Combined acoustical-electrical modeling for tight sandstones verified by laboratory measurements. *International Journal of Rock Mechanics and Mining Sciences, 176*, 105682. https://doi.org/10.1016/j.ijrmms.2024.105682

Tang, X. M. (2019). Experimental measurement and study on conduction mechanism and model for artificial matrix-conductive low resistivity samples (in Chinese).

Weerts, A., Kandhai, D., Bouten, W., & Sloot, P. (2001). Tortuosity of an unsaturated sandy soil estimated using gas diffusion and bulk soil electrical conductivity. Soil Science Society of America Journal, 65(6), 1577–1584. https://doi.org/10.2136/sssaj2001.6571577x

Worthington, P. F., & Pallatt, N. (1992). Effect of variable saturation exponent on the evaluation of hydrocarbon saturation. SPE Formation Evaluation, 7(4), 331–336. https://doi.org/10.2118/20538-PA

Corresponding author: han.yan@unito.it